LM-07K022
April 18, 2007

Nickel Alloy Primary Water Bulk Surface and SCC Corrosion Film Analytical Characterization and SCC Mechanistic Implications

D Morton, N Lewis, M Hanson, S Rice, P Sanders

NICKEL ALLOY PRIMARY WATER BULK SURFACE AND SCC CORROSION FILM ANALYTICAL CHARACTERIZATION AND SCC MECHANISTIC IMPLICATIONS

David Morton, Nathan Lewis, Michael Hanson, Steve Rice and Paul Sanders

Lockheed Martin Corporation
Schenectady, NY 12301-1072

Abstract

Alloy 600 corrosion coupon tests were performed: 1) to quantify the temperature dependency of general corrosion and 2) to characterize the composition and structure of bulk surface corrosion films for comparison with ongoing primary water SCC (PWSCC) crack tip corrosion film analyses. Results suggest that the thermal activation energy of Alloy 600 corrosion is consistent with the thermal activation energy of nickel alloy PWSCC. Analytical investigations of the structure and composition of Alloy 600 bulk surface corrosion oxides revealed a duplex (inner and outer) oxide layer structure. The outer layer is discontinuous and comprised of relatively large (1 to 3 μm) nickel ferrite crystals and smaller (~0.1 μm) chromium containing nickel ferrite crystals. The inner layer consists of a relatively continuous chromite spinel (major phase) and chromia (Cr_2O_3 minor phase) which formed through non-selective oxidation. Chromia and dealloyed Alloy 600 (highly Ni enriched metal) were only observed at 337°C (640°F) and only along the boundaries of deformation induced fine grains and subcells. Specimens having deformation free surfaces exhibited continuous uniform inner chromite spinel oxide layers. Specimens with machining induced surface deformation produced non-uniform inner layer oxides (chromite spinel, Cr_2O_3 and unoxidized material).

PWSCC crack tip oxides, in contrast, were fine grain (no duplex structure) and consisted of both chromium rich spinels and "NiO" structure oxides. Generally, nickel rich oxides were more abundant under more oxidized conditions (reduced coolant hydrogen) and spinel rich crack tip oxides were favored under more reducing conditions (increased coolant hydrogen). Bulk surface corrosion film thickness did not correlate with observed SCC growth rates. These results suggest that corrosion is not the rate controlling step of PWSCC but rather that PWSCC and corrosion have a common rate controlling sub process (e.g., cation diffusion, oxygen ingress).

1.0 INTRODUCTION

The mechanism of nickel alloy primary water stress corrosion cracking (PWSCC) has been extensively debated since 1959 when Couriou et al. [1] identified that Alloy 600 and other similar nickel alloys are susceptible to SCC. Many PWSCC key parameter dependencies suggest that corrosion/oxidation is a fundamental subprocess in the overall mechanism. PWSCC, for example, exhibits a maximum in susceptibility in a narrow ~ 100 mV corrosion potential window about the Ni/NiO phase transition [2], PWSCC shows a significant Arrhenius temperature thermal activation energy (Q) of ~33 kcal/mol [3] and chromium additions are known to be beneficial. Recent laboratory studies [4, 5] have been performed to characterize the morphology and composition of oxides that form on nickel based alloys in primary water and to discern SCC mechanistic implications. These studies have identified that oxide composition and morphology are significantly influenced by the surface preparation (e.g., as-machined and electrochemically polished surfaces) and the material chromium content. Knowledge of the corrosion process of nickel based alloys in primary water is also essential in understanding the transport and buildup of radioactivity in primary water reactors (PWRs) coolant systems [4].

The primary goal of this corrosion study was to measure the temperature dependency of nickel alloy corrosion and to compare this functionality to the temperature dependency of PWSCC. The same temperature dependency of corrosion and PWSCC would indicate that the rate controlling step in PWSCC is corrosion or that PWSCC and corrosion have a common rate controlling subprocess. An additional goal of this study was to compare the corrosion product oxides which form on a smooth surface (this study) to corrosion oxides that are observed in nickel alloy primary water SCC initiation [6] and crack growth rate [7] tests.

A secondary goal of the corrosion study presented herein was to study the effect of material and surface condition on nickel alloy corrosion kinetics, oxide film morphology and composition. Specifically, in addition to Alloy 600, Alloy X-750 in the AH condition was tested. Furthermore, Alloy 600 was tested with five surface conditions, as-machined, as-machined and electropolished (ECP), as-machined and solution annealed, cold rolled, and cold rolled and electropolished.

2.0 TEST OUTLINE

Alloys 600 and X-750 condition AH corrosion coupon specimens were exposed in stainless steel autoclave facilities to hydrogenated water at either 550 or 640°F (288 and 338°C) for exposure times that varied between 500 and 5000 hours. Test condition details are presented below and are summarized in Table 1.

2.1 Test Specimens

Two types of corrosion specimens were employed, 'standard' corrosion coupons (4" x 3/4" x 0.032") and smaller coupons (5/8" x 3/4" x 1/16") used as Electron Spectroscopy for Chemical Analysis (ESCA) specimens. The ‘standard’ corrosion coupons were used to monitor corrosion behavior via a descale oxide removal and gravimetric analysis. ESCA specimen corrosion behavior was characterized by sequential ESCA analysis and ion milling.

TABLE 1a: Test Specimen Inventory and Exposure Durations for the 640°F Test Run

	Specimen Identification Numbers					
Material/Surface Condition/Coupon Type	500 hour exposure	1000 hour exposure	2000 hour exposure	3000 hour exposure	4000 hour exposure	5000 hour exposure
A600/ as-machined/standard	JD4-02,-03,-04	JD4-05,-06,-07	JD4-08,-09,-10	JD4-11,-12,-13	JD4-14,-15,-16	JD4-17,-18,-19
A600/ ECP/standard						JD4-21,-22,-23
A600/ as-machined/ESCA	HP4-01, -02	HP4-03, -04	HP4-05, -06	HP4-07, -08	HP4-09, -10	HP4-11, -12
Cold rolled A600/ CR as-machined/standard						JD6-02,-03,-04
Cold rolled A600/ CR-ECP/standard						JD6-06,-07,-08
A600/ solution annealed/standard					JD4-01,-29	
A600/ solution annealed/ ESCA					HP4-13,-14	
X-750/ as-machined/standard						JD5-01,-02,-03
X-750/ as-machined/ ESCA						HP5-01,-02

TABLE 1b: Test Specimen Inventory and Exposure Durations for the 550°F Test Run

	Specimen Identification Numbers					
Material/Surface Condition/Coupon Type	500 hour exposure	1000 hour exposure	2000 hour exposure	3000 hour exposure	4000 hour exposure	5000 hour exposure
A600/ as-machined/standard	JD4-47,-48,-49	JD4-50,-51,-52	JD4-53,-54,-55	JD4-56,-57,-58	JD4-59,-60,-61	JD4-62,-63,-64
A600/ ECP/standard						JD4-24,-25,-26
A600/ as-machined/ ESCA	HP4-19, -20	HP4-21, -22	HP4-23, -24	HP4-25, -26	HP4-27, -28	HP4-29, -30
Cold rolled A600/ CR as-machined/standard						JD6-20,-21,-22
Cold rolled A600/ CR-ECP/standard						JD6-09,-10,-11
X-750/ as-machined/standard						JD5-19,-20,-21
X-750/ as-machined/ ESCA						HP5-14,-15

2.2 Materials

Alloy 600 heat NX5805G11 and Alloy X-750 heat 38F3X in the AH condition were the materials which were tested. The composition of these materials is presented in Table 2. Alloy 600 was tested in the as-received 1800°F mill annealed condition as well as in a solution annealed and cold rolled conditions. The cold worked Alloy 600 specimens were fabricated from a 3.25"x13" by 2.261" thick block of Alloy 600 heat NX5805G11 which was cold rolled to 2.055" thickness in two passes. Both cold rolling passes were performed in the same direction as the original plate rolling. The solution anneal heat treatment was 2100°F for 20 minutes with a rapid inert gas quench.

TABLE 2: Material Composition for Alloys 600 and X-750 AH

Element	Alloy 600 Heat NX5805G11	X-750 AH Heat 38F3X
C	0.07	0.05
Mn	0.22	0.15
Fe	7.87	7.09
S	< 0.001	0.007
Si	0.21	0.24
Cu	0.20	0.23
Ni	75.77	72.60
Cr	15.04	15.75
Al	0.21	0.61
Ti	0.35	2.39
Mg	0.01	NR(1)
Co	0.04	0.05
P	0.007	NR
B	0.004	NR

(1) NR - not reported.

2.3 Surface Treatments

Alloy X-750 standard corrosion coupons were tested in the as-machined condition. All ESCA specimens had one side polished to a mirror finish using diamond paste to optimize the ESCA analyses.

In an effort to explore surface treatment effects, Alloy 600 corrosion coupons were tested with five different surface conditions, as-machined, as-machined and electrochemically polished, as-machined and solution annealed (SA), cold rolled, and cold rolled and electrochemically polished (ECP). The solution annealed and electrochemically polished specimen surfaces were expected to have surface residual stresses and microstrains (deformation) much less that those of the as-received and cold rolled specimens.

2.4 Water Chemistry

Tests were conducted at 550 and 640°F (288 and 338°C) in deaerated high purity water with dissolved hydrogen. The feed tank solution in each test was buffered to a room temperature pH of 10.1 to maintain a near neutral autoclave pH at the test temperatures. The feed water was sparged with hydrogen gas to remove dissolved oxygen. The 550°F test was operated at 18 cc/kg H_2 and the 640°F test was conducted at 60 cc/kg H_2. These hydrogen levels were selected to insure that the test corrosion potential relative to the corrosion potential of the Ni/NiO phase transition was constant (~37 mV into the nickel metal regime) at both test temperatures. Corrosion tests were conducted at a constant corrosion potential relative to the Ni/NiO phase transition since nickel alloy SCC temperature dependency evaluations are performed holding this parameter constant. Nickel alloy PWSCC follows an Arrhenius temperature dependency and resulting thermal activation energies are biased if testing is not conducted at a constant corrosion potential relative to the Ni/NiO phase transition [3].

3.0 RESULTS and DISSCUSION

3.1 Pretest X-Ray Diffraction Residual Stress and Micro-Strain Analyses

X-ray diffraction pretest surface residual stress and micro-strain measurements were made to characterize the surface condition of the five Alloy 600 test surface treatments. Results from these X-ray diffraction analyses are summarized in Table 3.

Table 3: X-ray Diffraction Characterization of Surface Residual Stress and Micro-Strain for Alloy 600 Test Specimen Surface Treatments

Surface Treatment	"Micro-Strain" 220 FWHM[(i)] (°)	Residual Longitudinal Stress (ksi)	Residual Shear Stress (ksi)	Residual Transverse Stress (ksi)
As-machined (JD4-01)	1.43	-26.7 ± 1.8	-7.7 ± 1.8	-38.9 ± 1.8
Cold rolled (JD6-01)	1.13	-17.5 ± 1.4	2.8 ± 1.4	-35.7 ± 1.4
As-machined and ECP (JD4-20)	0.79	0.6 ± 1.4	6.0 ± 1.4	35.1 ± 1.4
Cold rolled and ECP (JD6-05)	0.85	5.8 ± 2.2	3.2 ± 2.2	-5.7 ± 2.2
Solution Annealed (SA) (JD4-28)	ND[(ii)]	ND	ND	ND
Tensile Specimen SA after machining (GL5-60)	0.9	-4.1 ± 3.8	6.5 ± 3.8	-5.9 ± 3.8
Tensile Specimen SA before machining (GL5-118)	2.09	94 ± 4.6	-32.3 ± 4.6	-19.4 ± 4.6

[(i)] Because all samples started from the same heat of material they would have had similar starting grain structure. An increase in the full width half maximum (FWHM), which is a measure of X-ray

diffraction peak broadening, indicates an increase in the micro-strain/deformation. The FWHM for Alloy 600 power which has negligible micro-strain/deformation is 0.54.

(ii) The diffraction cones from the solution annealed Alloy 600 corrosion coupon were spotty and did not permit residual stress and micro-strain analysis. The diffraction pattern from this specimen indicates that the sample has very large grains and a very small quantity of defects/deformation.

X-ray diffraction results indicate that as-machined and cold rolled specimens have greater deformation and residual stresses compared to the solution annealed and electrochemically polished specimens. The solution anneal (SA) heat treatment removes machining deformation by recovery and recrystallization of deformed grains. In contrast, electrochemically polishing (ECP) literally removes the material comprising the machining surface deformation layer. Machining processes, in general, leave a compressive (negative sign) residual surface stress(1) as was observed with the as-machined and cold rolled specimens. The slightly higher FWHM of the as-machined specimen compared to the as-machined cold rolled specimen indicates that surface microstrain/deformation induced by machining overwhelms the micro-strain that is induced by cold rolling. The minimal micro-strain measured on the cold rolled and ECP specimen (0.85) also supports this conclusion.

Also reported in Table 3 are X-ray diffraction results for two solution annealed tensile specimens which were tested at 620°F (327^{0}C) in 14 cc/kg dissolved hydrogen primary water for 99 days as part of a stress corrosion crack initiation testing study [6]. An important distinction between these two specimens was that GL5-60 was solution annealed after machining and GL5-118 was solution annealed before machining. As a result, analogous to the corrosion coupons, the surface residual stress and micro-strain were far less in the specimen which was annealed after machining.

3.2 Optical Inspection Results

Representative optical photographs of the test specimens are provided in Figures 1 and 2. These low magnification photographs capture the post-test oxide film heat tint coloration. Generally, darker heat tints imply thicker corrosion films. Figure 1 compares specimens with different surface conditions (SA, ECP, as-machined and cold rolled). Figure 2 compares as-machined (AM) specimens tested at different temperatures and different exposure times. As shown in these figures, all specimens developed a heat tint. A dark gray heat tint formed on as-machined and cold worked specimens exposed to 640°F primary water for 4000/5000 hours. In comparison gold/brown heat tints formed on as-machined specimens exposed for a similar duration at 550°F and for 500 hours at 640°F, Figure 2. This data qualitatively indicates that increased exposure times and increased temperatures give rise to thicker corrosion films. The heat tints of the Alloy X-750 AH specimens look analogous to their counterpart Alloy 600 specimens.

A speckled brown/gray heat tint was observed on the SA Alloy 600 specimen exposed at 640°F for 4000 hours and a speckled gold/brown heat tint was observed on the ECP Alloy 600 specimen

(1) During machining processes the surface is plastically deformed more than the core of the material. Consequentially, the surface work hardens to a greater extent than the core which prevents the core from completely recovering elastically. The elastic stress maintained within the core of the material is the residual stress.

Figure 1: Comparison of Optical Heat Tints on Alloy 600 Specimens with Different Surface Treatments. Darker oxides generally indicate thicker corrosion films.

JD4-28	JD4-01	JD4-22	JD4-17	JD4-04
SA A600	SA A600	ECP A600	AM A600	Cold worked A600
Not Tested	4000 hours, 640F	5000 hours, 640F	5000 hours, 640F	5000 hours, 640F

Figure 2: Comparison of Optical Heat Tints on As-Machined (AM) Alloy 600 Specimens with Different Exposure Times and Temperatures.

HP4-01	HP4-28	HP4-10
AM A600	AM A600	AM A600
640°F, 500 hrs	550°F, 4000 hrs	640°F, 4000 hrs

exposed at 640°F for 5000 hours. These results indicate that the SA and ECP surface treatments reduce the rate of corrosion. The speckled appearance occurs because the Alloy 600 grain structure is visible in the ECP and SA specimens and oxidation was not extensive enough to entirely obscure the grain structure. Cold worked-ECP specimen oxide films were analogous to non-cold worked

ECP specimen oxide films and cold worked-machined specimen oxide films were analogous to as-machined specimen oxide films.

3.3 SEM Inspection Results

Figures 3-7 provide representative scanning electron microscope (SEM) photographs characterizing the extent of outer layer oxide buildup as a function of surface condition, exposure time and exposure temperature. Figure 3 compares two as-machined specimens exposed at 640°F for 500 and 4000 hours. As illustrated in Figure 3, well formed polyhedral crystals formed under both exposure periods. There was no preferential orientation relationship observed between the oxide crystals and the underlying substrate. As discussed below X-ray diffraction and energy dispersive spectroscopy (EDS) analyses confirmed that these large crystals are a nickel rich ferrite with trace amounts of chromium. The smaller crystals tended to be more chromium rich.

Figure 4 compares sister as-machined Alloy 600 specimens tested at 550 and 640°F for 4000 hours. The effect of temperature on the outer oxide crystal morphology and size distribution is less pronounced than the effect of exposure time noted in Figure 3. The most apparent difference between the 550 and 640°F outer layers was a slightly greater number density of large crystals at elevated temperature.

Figures 5 and 6 provide SEM inspection results for an ECP specimen tested at 640°F for 5000 hours and Figure 7 provide results for a SA specimen tested at 640°F for 4000 hours. The outer layer crystal morphology of the SA and ECP specimens was similar. In both cases the underlying surface grain structure was apparent. Additionally, each SA and ECP specimen grain gave rise to a particular outer layer crystal orientation. Recall, as-machined specimens showed a random orientation of outer layer oxide crystals. This observed grain dependent crystal orientation indicates that the crystal nucleation occurs at the metal surface (i.e., heterogeneous nucleation).

The ferrite rich outer oxide layer forms from hydrothermal growth of iron ions diffusing to the metal oxide interface. The rate of outer layer ferrite growth is believed to be controlled by the solid state outward diffusion of iron ions through the protective inner layer oxide, [8]. The extent of overall outer layer growth is also dependent upon the dissolution of this layer which in turn is function of the coolant saturation, [9]. Negligible outer layer dissolution is expected to have occurred in this study since testing was performed in stainless steel autoclaves and the test solution was iron saturated.

Figure 6 provides a high magnification view of an Alloy 600 ECP specimen grain boundary. This photograph indicates that grain boundaries were etched by the ECP process and that preferential growth of oxide crystals occurs at grain boundaries. These results are consistent with prior results [4] which observed preferential grain boundary oxide growth in ECP specimens. This accelerated growth is likely due to greater outward cation (e.g., Fe^{+2}) transport along grain boundaries compared with bulk transport rates.

Figure 3: SEM Images Comparing As-Machined Alloy 600 Specimens Exposed to 640°F Hydrogenated Water for 500 and 4000 hours.

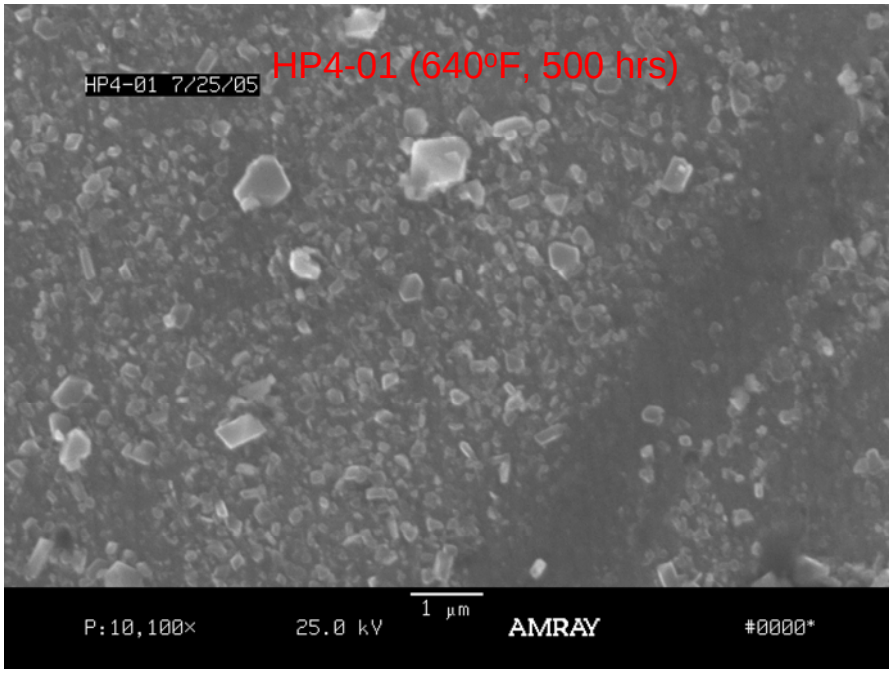

a) 500 hour exposure

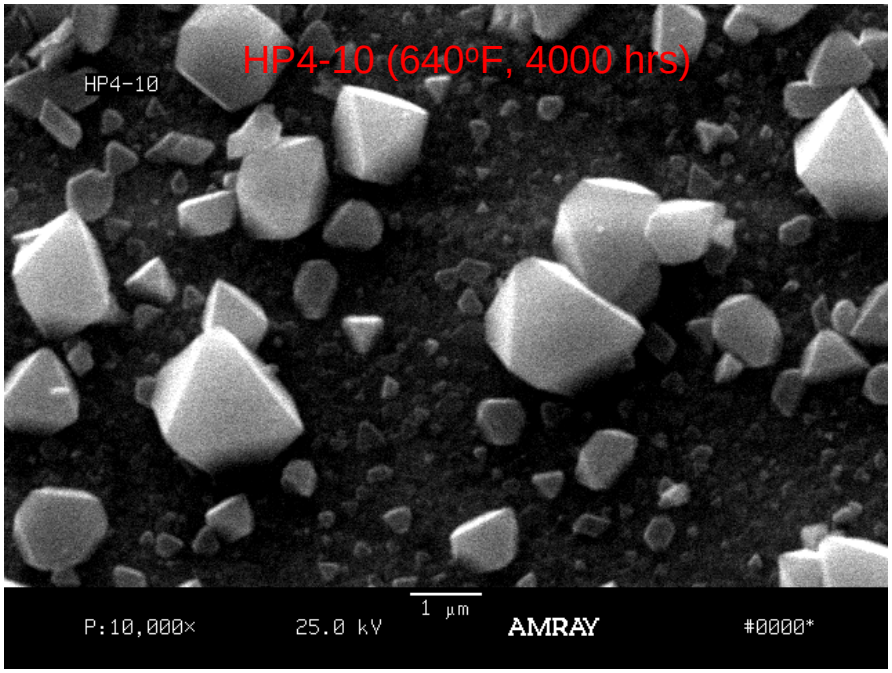

b) 4000 hour exposure

Figure 4: SEM Images Comparing As-Machined Alloy 600 Specimen Exposed to 550°F and 640°F Hydrogenated Water for 4000 hours.

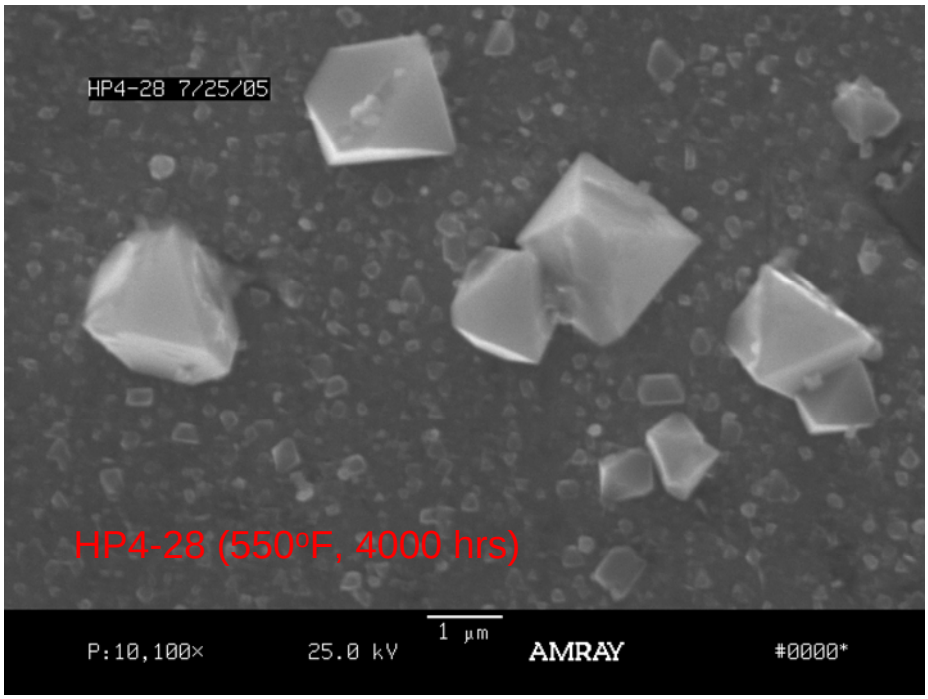

a) 550°F for 4000 hours

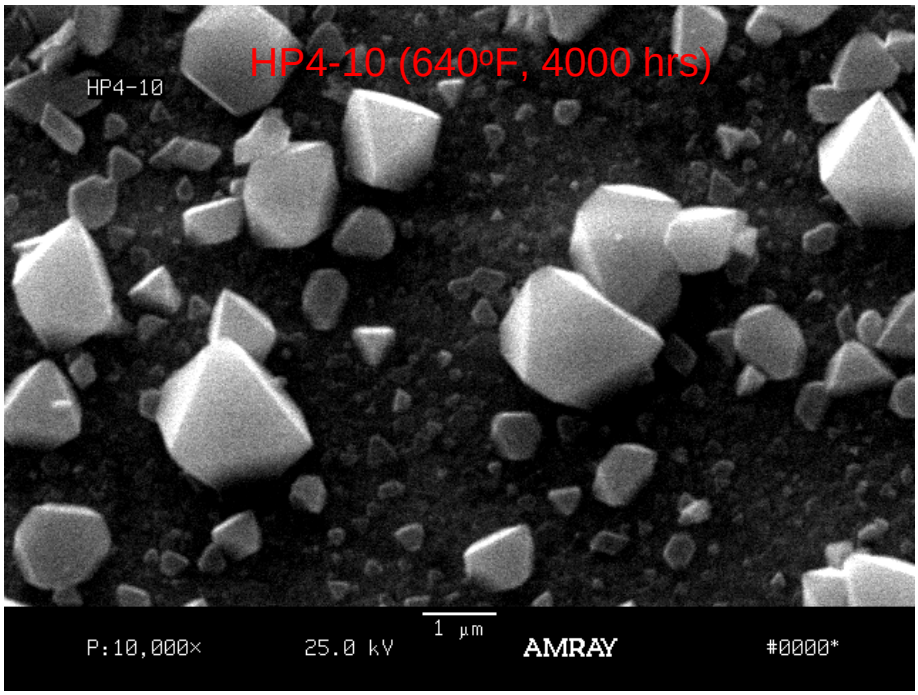

b) 640°F for 4000 hours

Figure 5: SEM Images of an Electrochemically Polished Alloy 600 Specimen Exposed to 640°F Hydrogenated Water for 5000 hours.

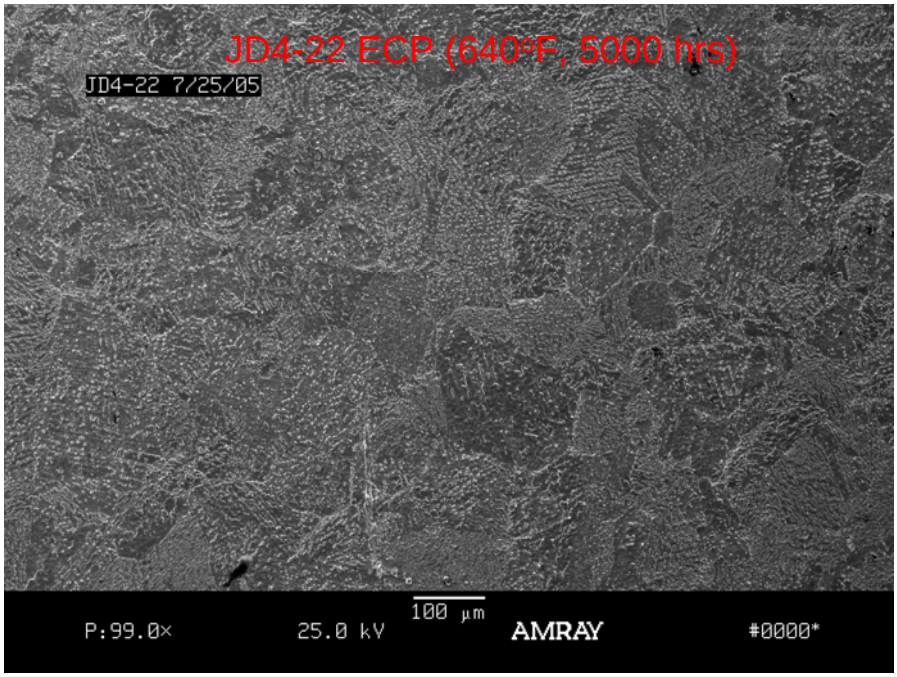

a) Low magnification image showing the underlying grain structure

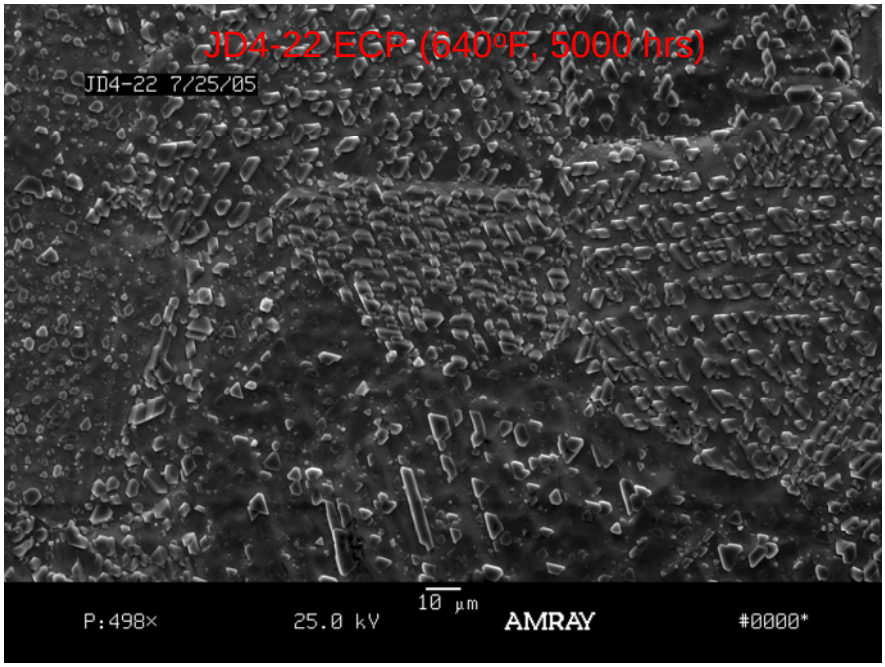

b) Higher magnification image indicates that the outer layer ferrite crystals exhibit preferred growth orientations related to the grain in the underlying substrate

Figure 6: High Magnification SEM Image of an Electrochemically Polished Alloy 600 Specimen Exposed to 640°F Hydrogenated Water for 5000 hours. Image shows increased oxide crystal growth at a grain boundary.

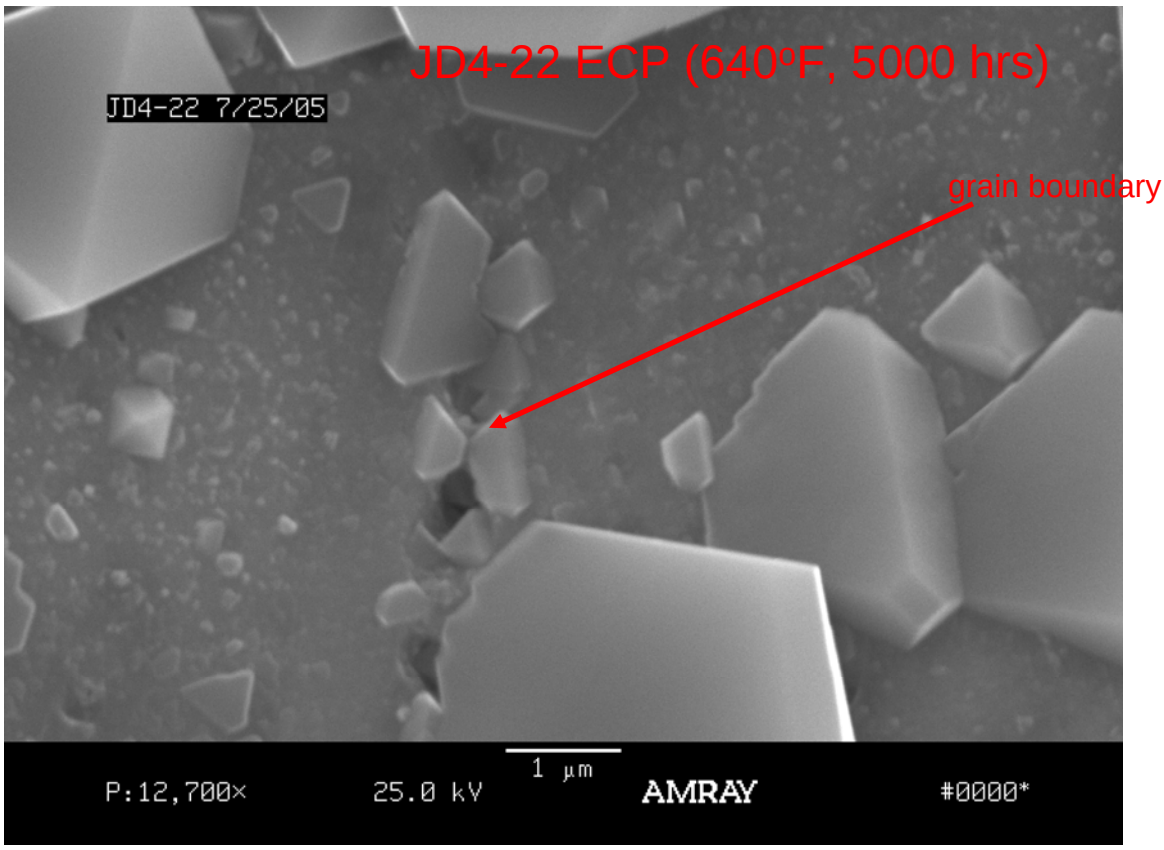

Figure 7: SEM Image of a Solution Annealed Alloy 600 Specimen Exposed to 640°F Hydrogenated Water for 4000 hours.

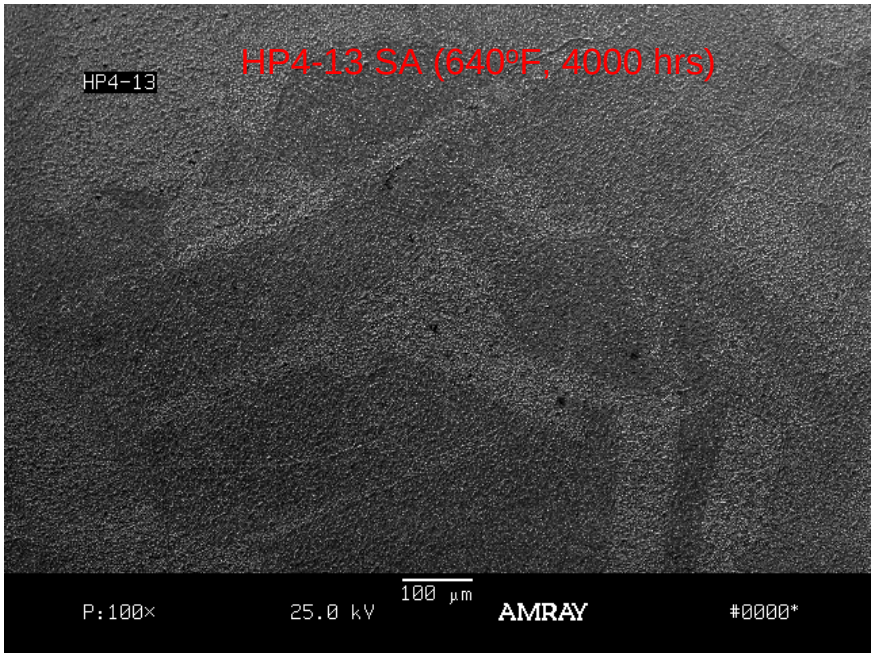

a) Low magnification image showing the underlying grain structure

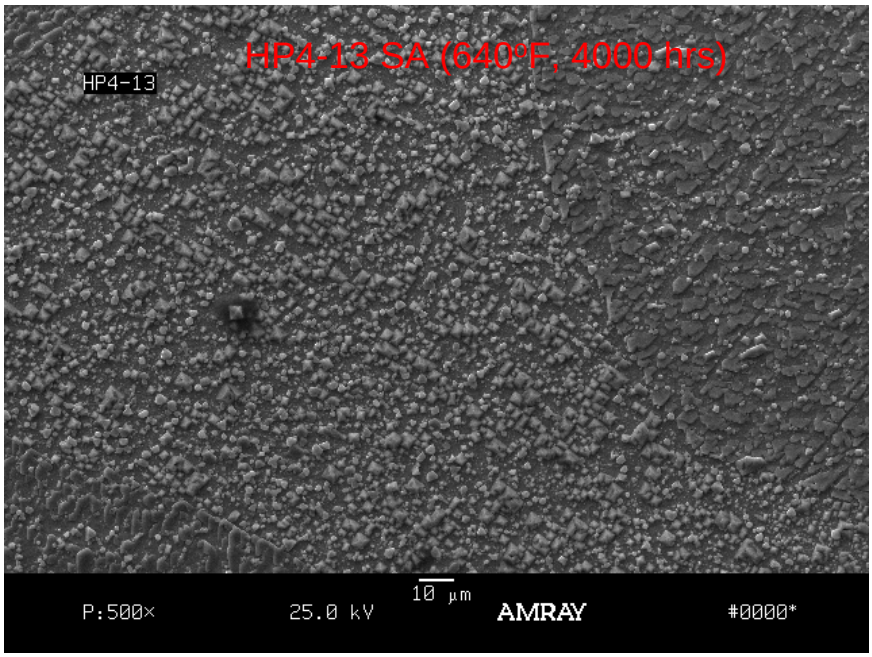

b) Higher magnification indicates that each grain nucleated a particular outer layer ferrite crystal oxide orientation

3.4 Analytical Electron Microscope Oxide Composition and Structure Determination

Analytical electron microscope (AEM) inspections of specimen oxide film cross sections indicate that the oxide layer that forms on Alloy 600 when it is exposed to hydrogenated primary water consists of two layers; an outer ferrite spinel and an inner chromium rich oxide. Consistent with SEM results, the outer layer is comprised of large 1 to 3 μm nickel rich ferrite crystals and smaller (~0.1 μm) more chromium rich ferrite crystals. The inner layer consists of fine grain chromium rich oxides. As discussed below, solution annealed and electrochemically polished specimens showed an inner layer with uniform composition with no evidence of selective oxidation whereas evidence of selective oxidation was observed in isolated inner layer regions of as-machined specimen. The overall data, however, suggests that the oxidation occurred via a non-selective oxidation process.

3.4.1 Electrochemically Polished and Solution Annealed Specimens

A representative low magnification AEM image of the oxide layers that formed on an electrochemically polished Alloy 600 specimen exposed to 640°F primary water for 5000 hours is presented in Figure 8. The inner chromium rich oxide layer completely covered the Alloy 600 substrate and had a relative uniform thickness of ~ 0.1 μm.

Figure 8: Low Magnification AEM Image of an Electrochemically Polished Specimen Exposed to 640°F Hydrogenated Water for 5000 hours.

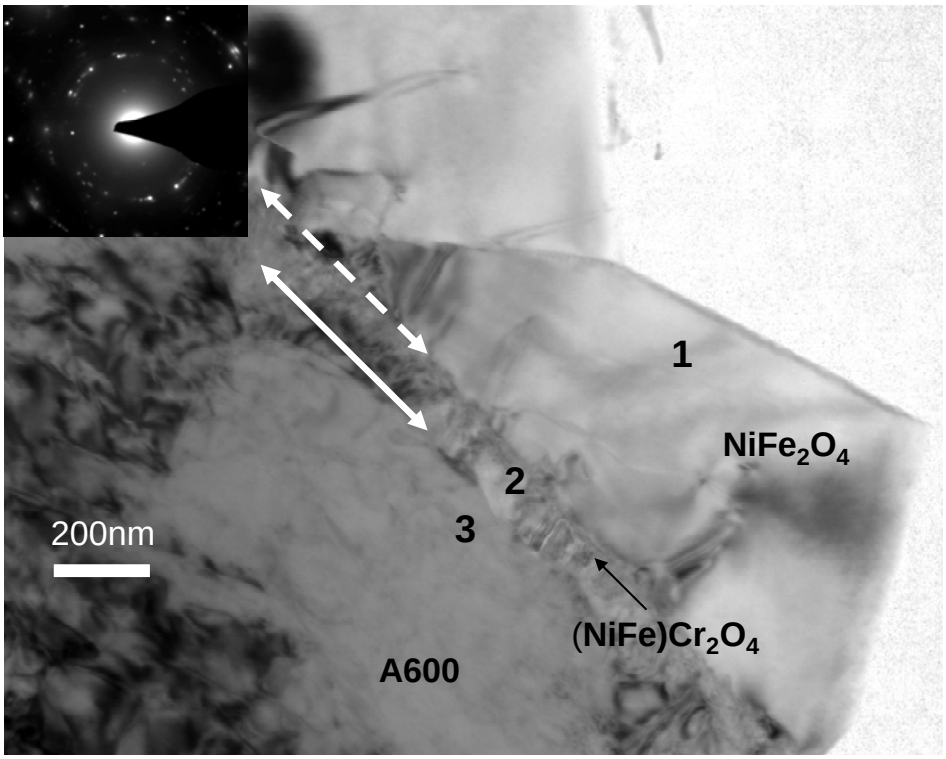

AEM electron diffraction analysis and grazing incidence X-ray diffraction confirmed that the large outer layer crystals were a nickel rich ferrite and the inner layer was a chromium rich spinel. The actual lattice size was between $NiCr_2O_4$ and $NiFe_2O_4$. Energy dispersive spectroscopy analysis of

the inner and outer layer oxide films suggests inner and outer non-stoichiometric oxide layers compositions of $Ni(Cr_{0.5}Fe_{0.5})_2O_4$ and $(Ni_{0.9}Fe_{0.1})Fe_2O_4$, respectively.

These results are consistent with results from a prior 680°F (360°C) study [4], except that a thin Cr-rich layer (assumed to be Cr_2O_3) was observed beneath the chromium rich spinel. Nickel enrichment was also observed at the metal/oxide interface in the Reference [4] study. The presence of Cr_2O_3 and the dealloyed region beneath the chromia is suggestive of a selective oxidation process (i.e., chromium is oxidizing more readily than the other alloy constituents). Extensive efforts were employed in this study to identify the possible presence of Cr_2O_3 and nickel enrichment at the metal oxide interface. However, neither Cr_2O_3 nor nickel enrichment was observed at the oxide metal interface, of electrochemically polished and solution annealed specimens. Figure 9, for example, provide representative AEM line scan data: 1) confirming the duplex spinel layer oxide structure and 2) showing no evidence of an additional Cr_2O_3 layer or associated nickel metal enrichment at the metal/oxide interface.

Figure 9: AEM Line Scan of an Electrochemically Polished Specimen Exposed to 640°F Hydrogenated Water for 5000 hours.

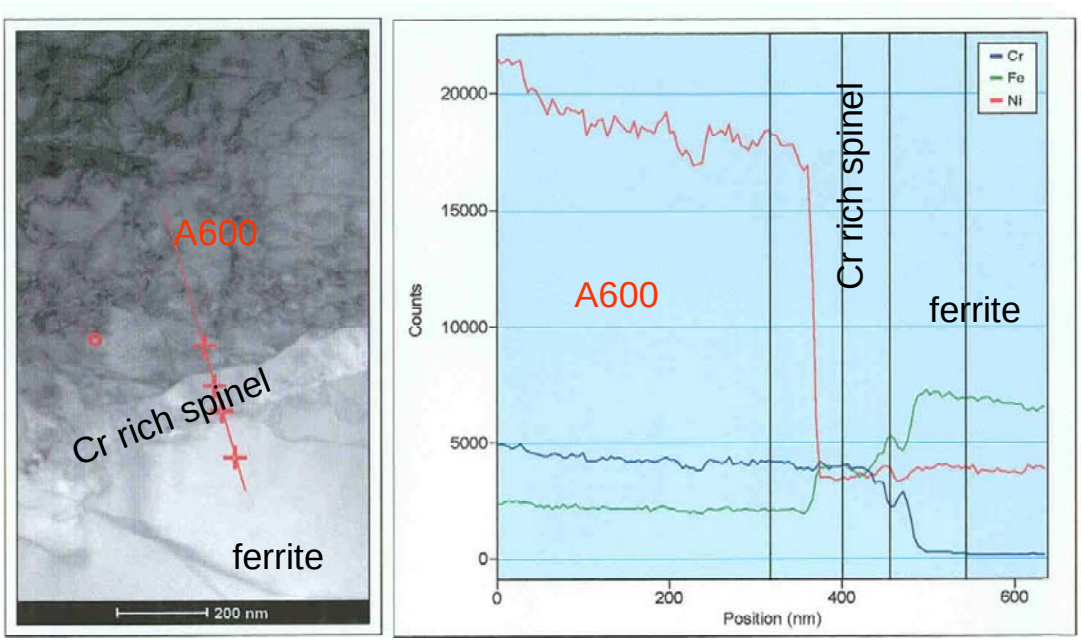

The composition and structure of oxide films which formed on solution annealed specimens were analogous to those that formed on the electrochemically polished specimens. Figure 10 provides a representative AEM image which shows the duplex layer spinel oxide structure on a solution annealed specimen. AEM line scan results, Figure 11, indicate that no Cr_2O_3 or nickel metal enrichment is seen at the metal/oxide interface. The only difference noted between SA and ECP specimen oxide films was that chromium enrichment was noted between the ferrite and chromite spinel layers in the SA specimens. The chromium enrichment at this location is unusual in films grown in hydrogenated water. This region is suspected to have originated during the specimen solution annealing heat treatment. This region is believed to delineate the original (pretest) outermost test specimen surface.

Figure 10: Low Magnification AEM Image of a Solution Annealed Specimen Exposed to 640°F Hydrogenated Water for 4000 hours.

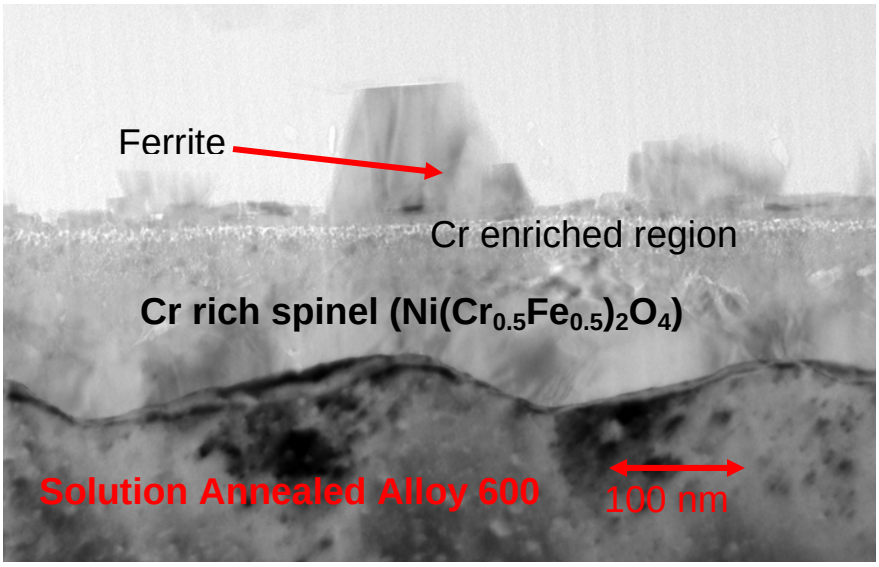

Figure 11: AEM Line Scan of a Solution Annealed Specimen Exposed to 640°F Hydrogenated Water for 4000 hours (Scan was in a region between outer layer ferrite crystals).

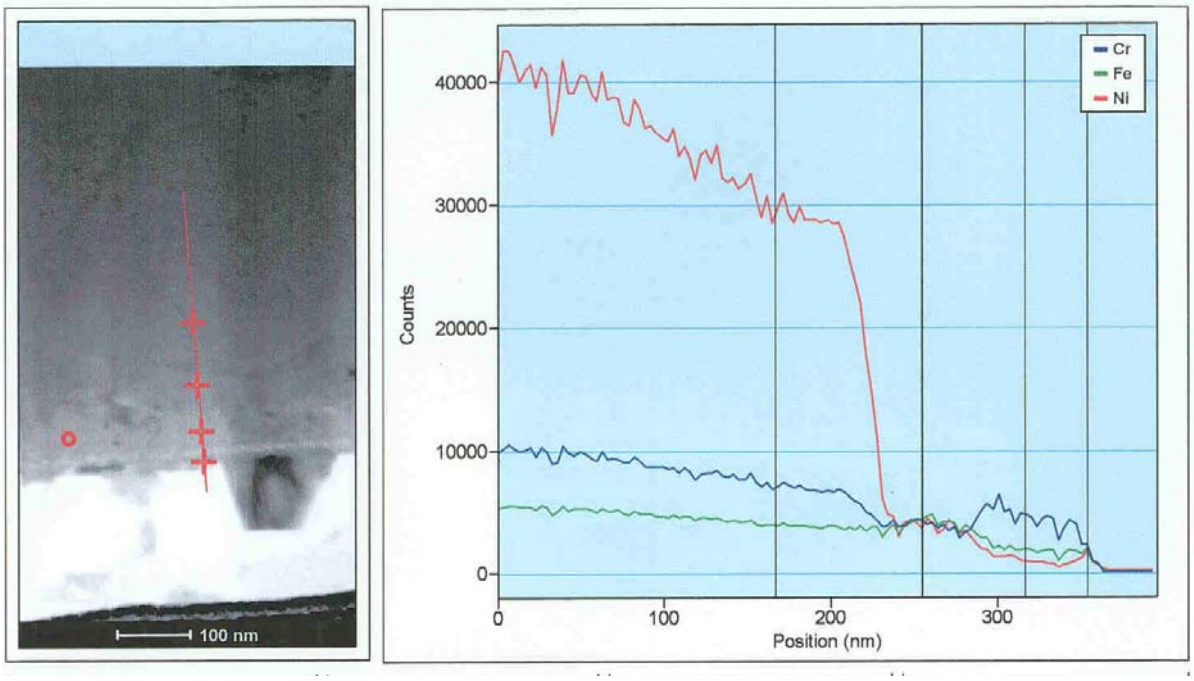

3.4.2 As- Machined Specimens

Analogous to the SA and ECP specimens, large ferrite crystals are the outermost oxide layer on as-machined specimens, Figure 12. Unlike SA and ECP specimen ferrite crystals, as-machined specimen ferrites were not preferentially orientated with the underlying substrate and were not very adherent. (The large crystals were easily rubbed off).

The composition and structure of the inner oxide layer of the as-machined specimens was dramatically different from what was observed on the SA and ECP specimens. A uniform chromium rich spinel oxide layer was not observed. In contrast, the inner oxide layer consisted of a layer intermixed with oxidized, unoxidized and dealloyed material. Unlike the SA and ECP specimens which had a deformation free outer surface, the as-machined specimens had a highly deformed surface layer of 0.5 to 0.75 μm thickness with a very fine grain structure including deformation subcells. As shown in the AEM images (Figures 12-14), the deformed metal surface layer was not uniformly oxidized. Specifically, some small grain and subcell regions were oxidized and other adjacent small grain and subcell regions were not. The major phase of oxidized material was indexed by X-ray diffraction as a non-stoichmetric nickel chromite in both the 550 and 640^{o}F test specimens. A minor phase of Cr_2O_3 was noted in the 640^{o}F specimens and a minor chromium rich oxide phase (possibly a non-stoichiometric form of CrO(OH)) was observed in the 550^{o}F specimens. In general, oxide was observed throughout the entire depth of the deformation layer. The presence of isolated Cr_2O_3 pockets in the as-machined specimens but not in the SA and ECP specimens is consistent with gaseous oxidization results which indicated that chromia nucleates more readily within machined surfaces compared to ECP surfaces due to faster diffusion of Cr along the many metal subcell and small grain boundaries within the deformed surface layer [8].

Figure 13 shows an AEM image with corresponding X-ray spectra from the highly deformed surface layer. The X-ray spectra show the large variation in elemental constituents within this layer that include small grains of unreacted Alloy 600, dealloyed Alloy 600 (highly Ni enriched metal), spinels (Ni ferrite and Ni chromite) and Cr_2O_3. These results suggest the preferential oxidation of chromium in select regions. That is, the fine grain chromium rich oxide formed by dealloying the adjacent Alloy 600. These observations are somewhat consistent with the Reference [4] observations of a thin layer of Cr_2O_3 at the metal/oxide interface with nickel enrichment beneath the oxide. The presence of a uniform layer of Cr_2O_3 at the metal/oxide interface with nickel enrichment beneath the oxide is indicative of a selective oxidation process. *However, in this study a uniform layer of chromia (*Cr_2O_3*) was not present indicating that the oxidation occurred by non-selective oxidation.*

Figure 12: Low Magnification AEM Image of an As-Machined Specimen Exposed to 640°F Hydrogenated Water for 5000 hours.

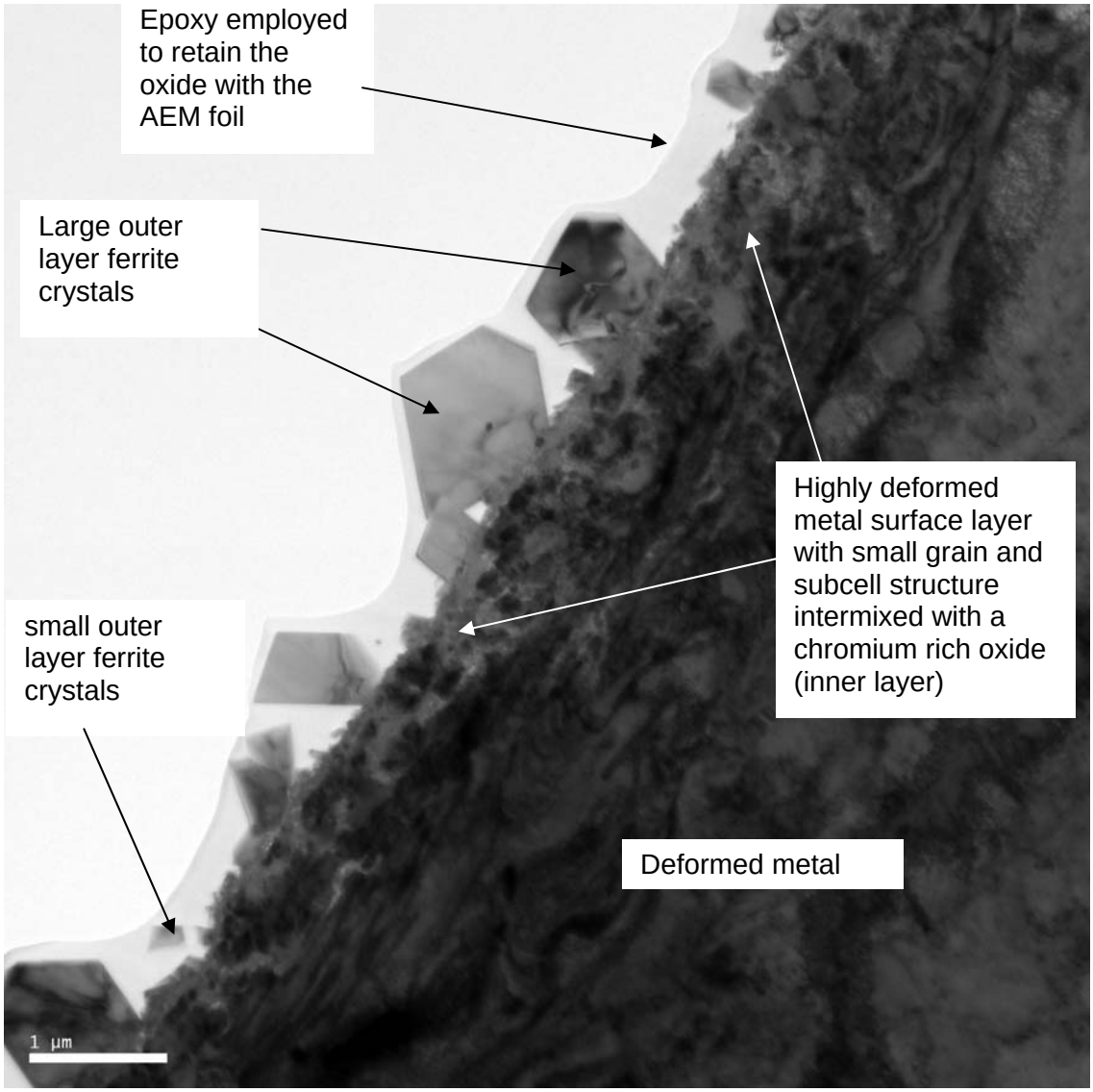

Figure 13: AEM Photograph of an As-Machined Specimen Exposed to 640°F Hydrogenated Water for 5000 hours.

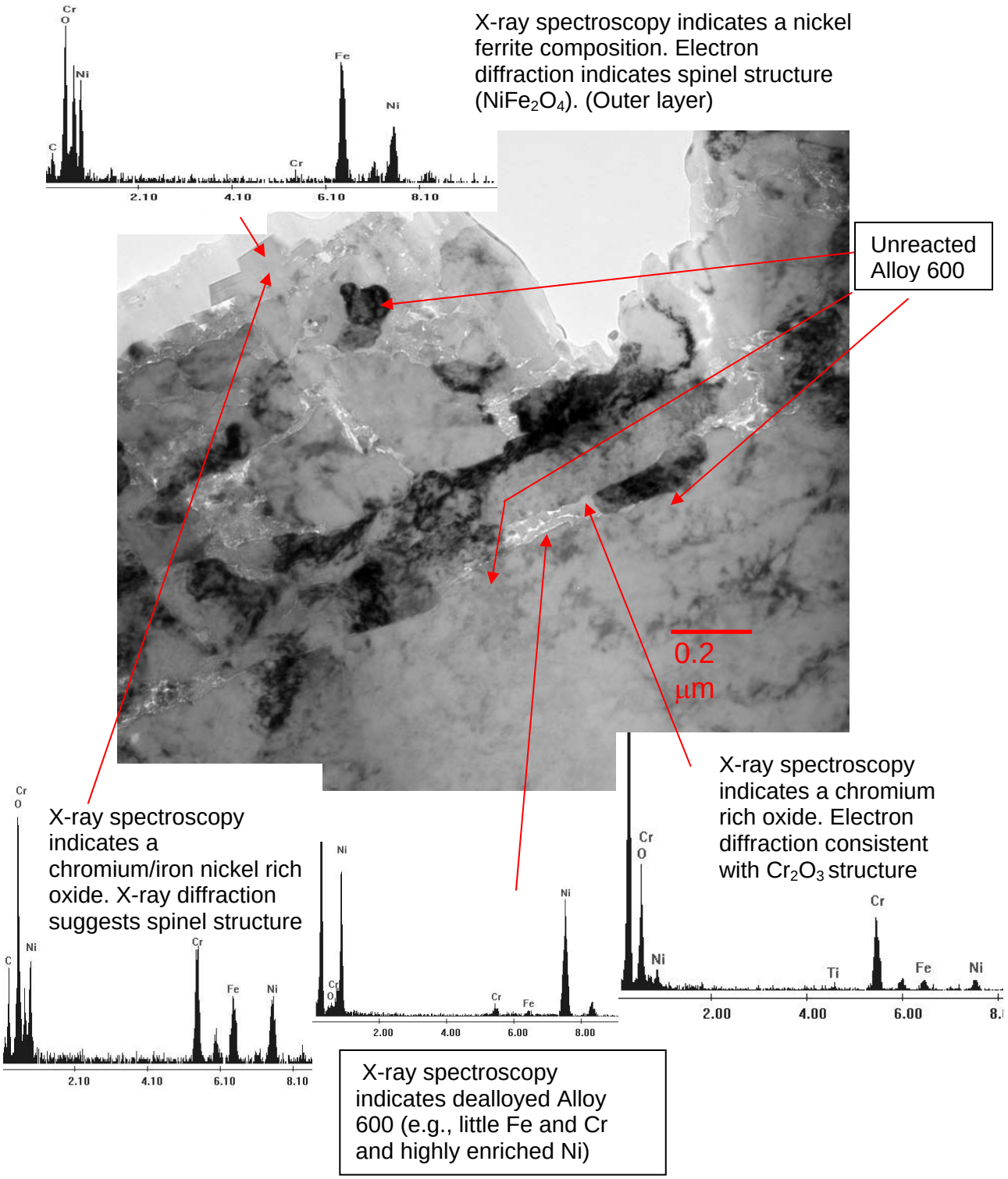

Figure 14: AEM Image of the Fine Grain Chromium Rich Inner Oxide Layer that Formed on an As-Machined Specimen Exposed to 550°F Hydrogenated Water for 5000 hours.

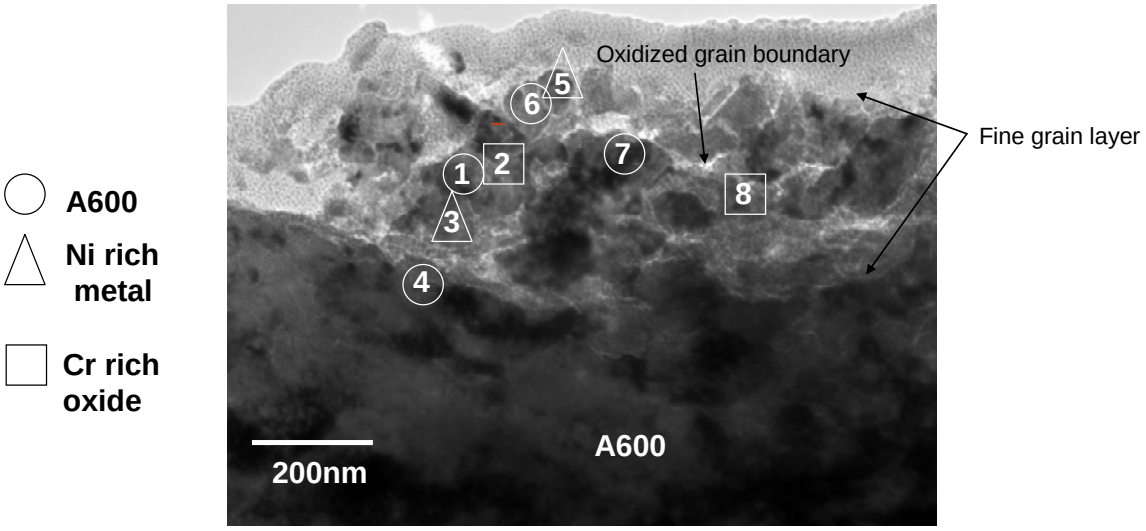

3.5 Electron Spectroscopy for Chemical Analysis (ESCA)

Representative Electron Spectroscopy for Chemical Analysis (ESCA) inspection results of as-machined specimens exposed to primary water for 5000 hours at 640 and 550°F are presented in Figures 15 and 16, respectively. Each ESCA depth profile provides the composition and oxidation state of key elemental species as a function of depth from the outermost surface. For each as-machined specimen, two ESCA inspections were performed: one with the outer ferrite layer present (Figures 15a and 16a) and one with the outer ferrite layer removed[2] (Figures 15b and 16b). Comparisons between the ESCA results with and without the outer oxide layer revealed that the outer ferrite rich layer was much thicker than the inner layer. As summarized in Table 4, the outer layer oxide thickness was roughly 5 times thicker than the inner layer oxide thickness.

Table 4: ESCA Determined Oxide Film Thickness for As-Machined Specimen Exposed to Primary Water for 5000 Hours

Test Temperature	Overall Oxide Thickness (μm)	Inner Layer Oxide* Thickness (μm)	Outer "Ferrite" Oxide Thickness (μm)
550°F	0.16	0.03	0.13
640°F	1.42	0.22	1.20

* ESCA oxide film thickness measured with the outer ferrite layer removed (Figures 15b and 16b).

[2] The ferrite rich outer oxide layer was removed by mechanically rubbing the specimen with an eraser. SEM inspections revealed that the ferrite layer removal procedure was effective for the as-machined specimens (loosely adherent) but not effective for the electrochemically polished and solution annealed specimens (tightly adherent).

Figure 15: ESCA Oxide Depth Profile of an As-Machined Specimen Exposed to 640°F Hydrogenated Water for 5000 hours.

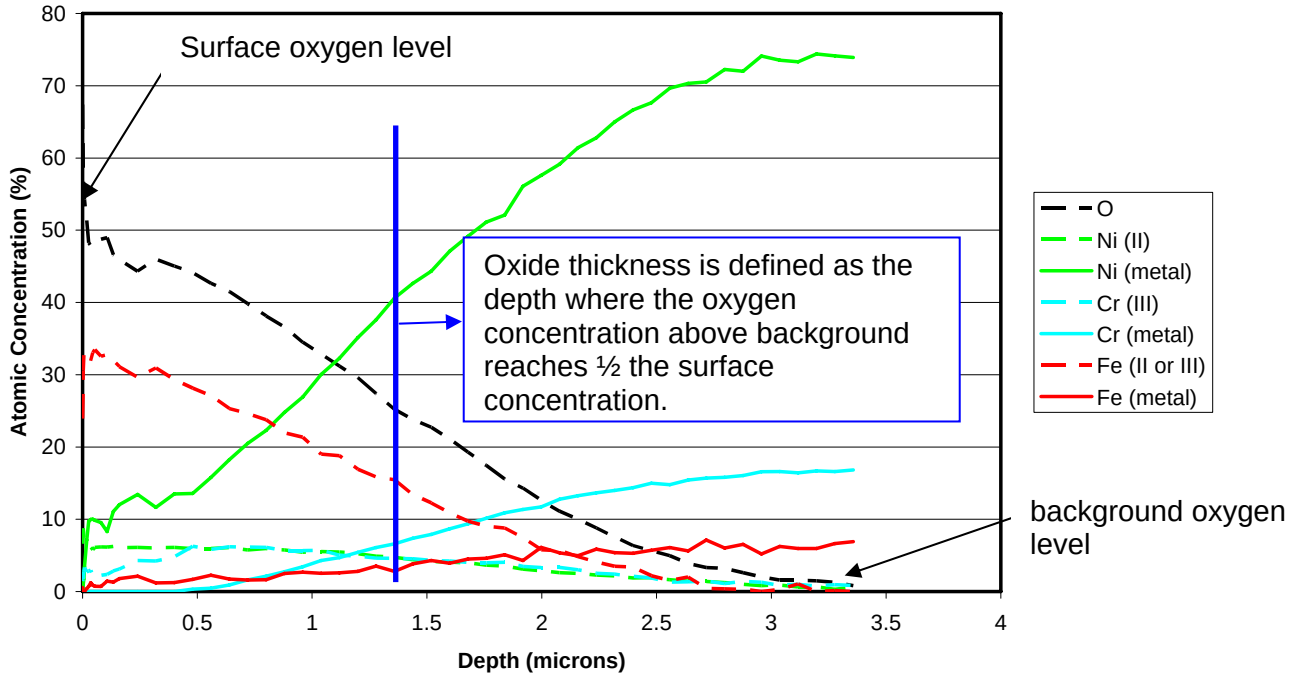

a) depth profile with the ferrite outer layer present

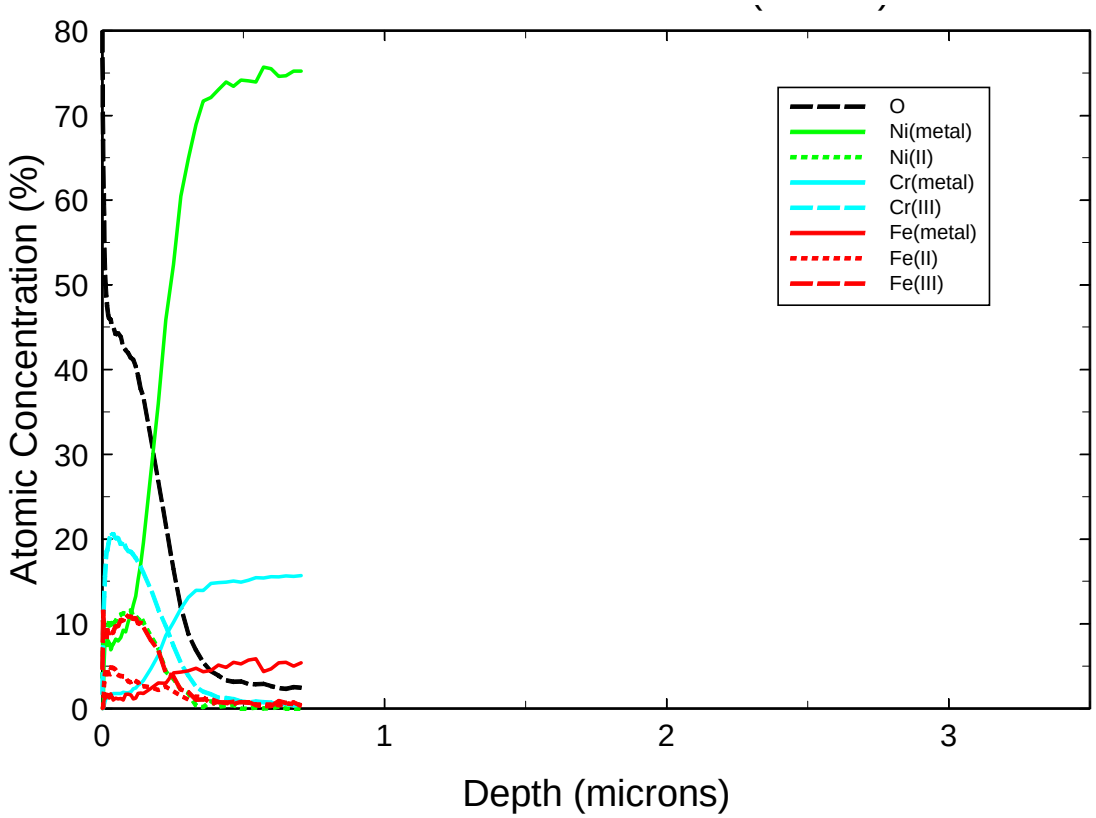

b) depth profile with the ferrite outer layer removed

Figure 16: ESCA Oxide Depth Profile of an As-Machined Specimen Exposed to 550°F Hydrogenated Water for 5000 hours.

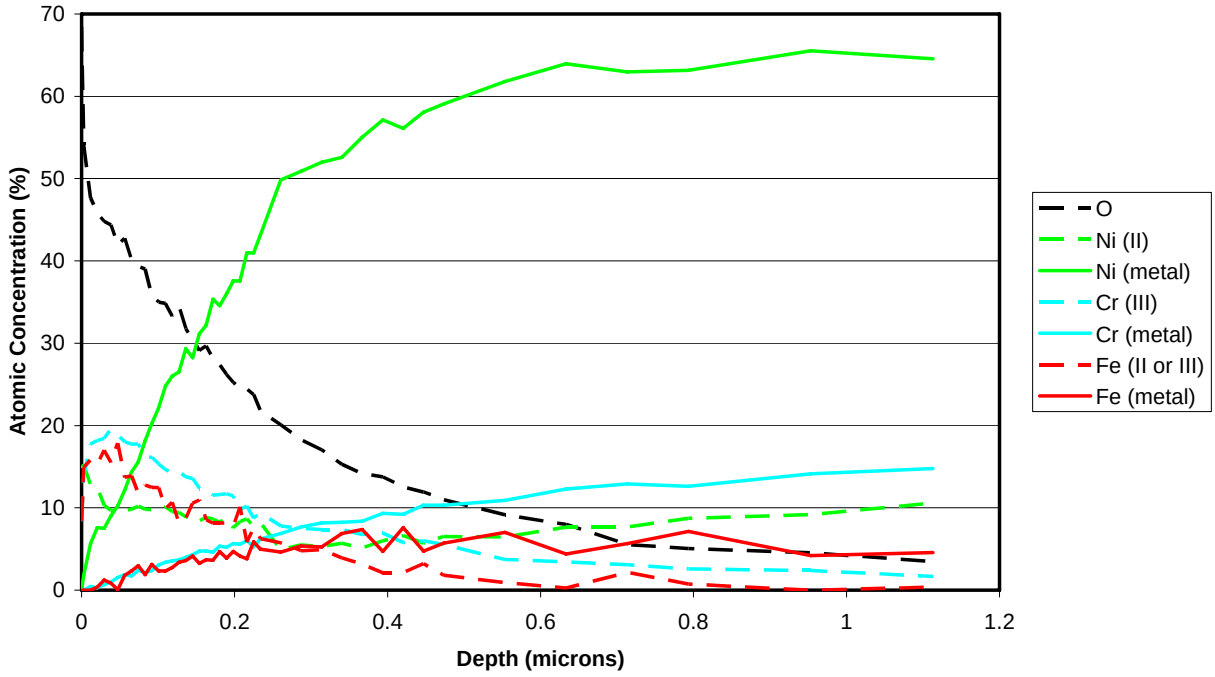

a) depth profile with the ferrite outer layer present

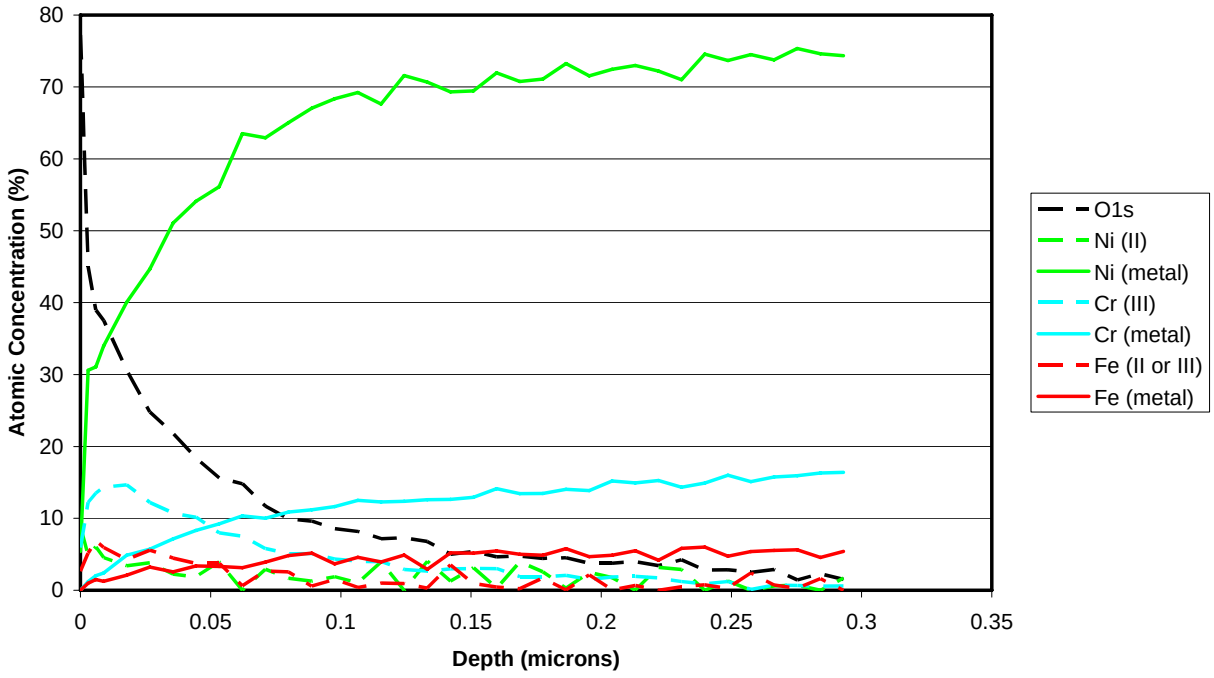

b) depth profile with the ferrite outer layer removed

3.5.1 Thermal Activation Energy (Q) Evaluation

The plan going into this study was: 1) to generate oxide thickness parabolic rate constants at each test temperature from gravimetric analyses of oxide descale data and ESCA evaluations of as-machined specimens and 2) to compare these constants to determine the Arrhenius temperature dependency of Alloy 600 corrosion. As-machined specimen descale data, however, did not accurately characterize the material oxidation. Unfortunately, because of the non-uniform (intermixed oxidized and non-oxidized material) inner layer microstructure, the descale process removed both non-oxidized and oxidized material. Since this bias prevented the use of the descale data, corrosion kinetics were evaluated primarily through the ESCA test data.

The ESCA determined parabolic rate constants for the overall oxide thickness of as-machined specimens were 0.0150 ± 0.081 $\mu m/hr^{1/2}$ and 0.0013 ± 0.001 $\mu m/hr^{1/2}$ at 640^{o}F and 550^{o}F, respectively. These constants times the square root of the exposure time, in hours, provides the oxide thickness in microns. A thermal activation energy (Q) of 33.2 ± 13 kcal/mol was obtained from these measurements, see Table 5. Figure 17 illustrates that the parabolic rate constant data of this study is consistent with measurements at other test temperatures [8]. A Q of 29 kcal/mol was determined from an evaluation of rate corrosion constant data from this study and the Reference [8] data.

Other Alloy 600 corrosion thermal activation energy estimates, Table 5, were performed since concern existed as to validity of a parabolic rate constant. Parabolic corrosion kinetics are predicated on the assumption that diffusion through a uniform "growing" film is the rate controlling step. The assumption of a uniform diffusion barrier was questionable since the inner layer was not entirely oxidized. The Table 5 "integrated ESCA total oxidized material" and "gravimetric weight gain" data provides an independent verification of the temperature dependency obtained from the parabolic rate constants. Both these measurements show a corrosion temperature thermal activation of ~ 30 kcal/mol and both measurements did not rely upon the parabolic corrosion kinetic assumption. These overall oxidization estimates depend primarily upon the outer ferrite layer oxidation since outer layer oxide thicknesses are ~5X thicker than the inner layer thicknesses. The thermal activation energy determined from inner layer oxide depth measurements (25.7 ± 7 kcal/mol) is also consistent with 30 kcal/mol and this measurement should not be influenced by the outer ferrite layer. The only Table 5 thermal activation energy estimate that appreciably differed from 30 kcal/mol was the inner layer integrated oxidized Cr measurement of 15.8±4 kcal/mol. This result suggests that the oxidation of Cr may be controlled by a process different from that which is controlling the overall oxide growth (ferrite included). The growth of the overall oxide is likely controlled by the outward cation diffusion of iron and nickel through the developing chromium rich oxide [8]. The oxidation of chromium in contrast may be controlled by a different less temperature dependent process (e.g., oxidant ingress).

TABLE 5: Alloy 600 Corrosion Thermal Activation Determinations

Parameter Measured	ESCA Total Oxide Thickness From Parabolic Rate Constants	Integrated ESCA Total Oxidized Material[(a)]	Gravimetric Weight Gain	ESCA Inner Oxide Layer Thickness From Parabolic Rate Constants[(b)]	Integrated ESCA Inner Layer (erased) Oxidized Cr[(c)]
Measured Enhancement Ratio 640°F/550°F	0.0150 $\mu m/hr^{1/2}$/(0.0013 $\mu m/hr^{1/2}$)	10.4X	9.2X	0.0029 $\mu m/hr^{1/2}$/(0.00044 $\mu m/hr^{1/2}$)	3.2X
Thermal Activation Energy (kcal/mol)	33.2 ± 13	31.5 ± 9	30.3 ± 4	25.7 ± 7	15.8 ± 4

(a) The oxidized metal determined in ESCA depth profiles of non-erased specimens was integrated through the oxide depth to obtain the total oxidized material.

(b) Oxide depth measurements were made through the procedure identified in Figure 15 for specimens with the outer ferrite layer removed.

(c) The oxidized chromium determined in ESCA depth profiles of specimens with the outer ferrite layer removed was integrated through the oxide depth to obtain the inner layer integrated oxidized chromium level.

Figure 17: Comparison between Alloy 600 Parabolic Corrosion Rate Constants Measured in This Study and Reference [8].

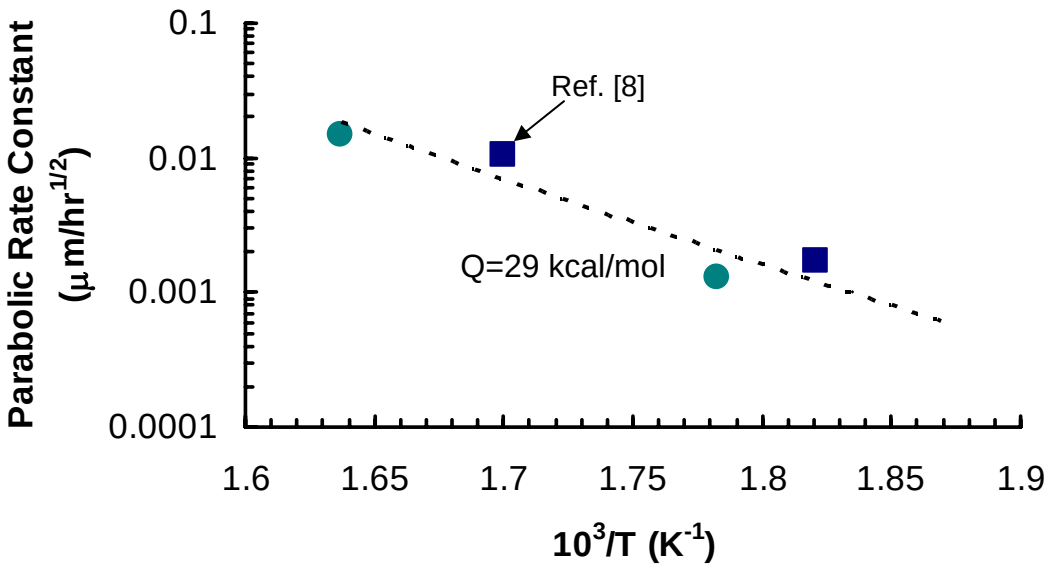

3.6 Comparison to SCC Oxide Films

3.6.1 SCC Initiation Specimens

AEM inspection of the corrosion films that form on Alloy 600 tensile SCC initiation specimens [6] revealed an oxide composition and morphology similar to that of the as-machined corrosion coupons. Specifically, a machining induced deformation surface layer of 0.5 to 1 μm was observed, Figure 18. Analogous with the as-machined corrosion coupons this deformation layer gave rise to an inner chromium oxide layer that was intermixed with oxidized material and non-oxidized material, Figure 19. The only significant difference that was observed between as-machined corrosion coupons and the tensile specimen oxide films was that in addition to outer layer spinel crystals, NiO was also observed in the outer layer, Figure 18. This difference was expected since the corrosion coupon study was performed well into the nickel metal regime whereas SCC initiation tests were performed at a hydrogen level corresponding to the Ni/NiO phase transition to maximize the SCC susceptibility [2].

Figure 18: AEM Cross-Sectional Image Showing the Corrosion Product Oxides which Formed on an Alloy 600 SCC Initiation Tensile Specimen Exposed to 680°F (360°C) High Purity Water with 30 cc/kg Dissolved Hydrogen for 1879 hours.

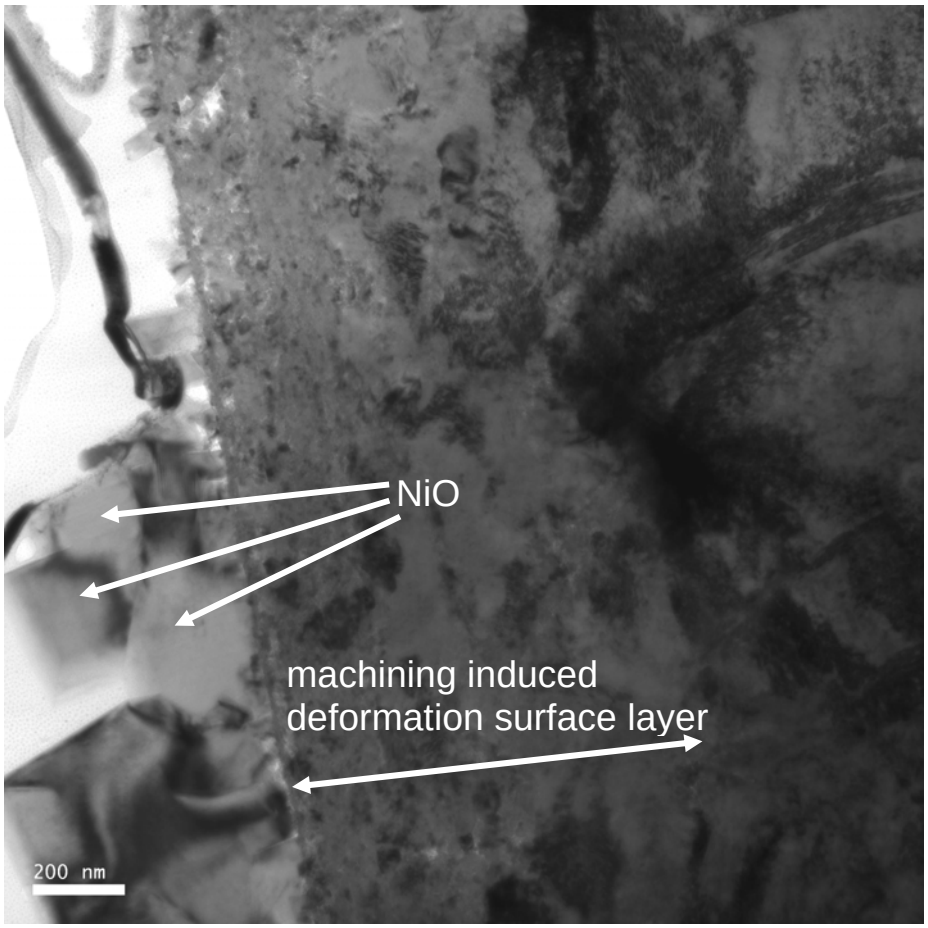

Figure 19: AEM Image of the Corrosion Product Oxides which Formed in the Inner Oxide Layer (heavily deformed layer) of an Alloy 600 SCC Initiation Tensile Specimen Exposed to 680°F (360°C) High Purity Water with 30 cc/kg Dissolved Hydrogen for 1879 Hours: Results show the inner layer is intermixed with oxidized, dealloyed and unoxidized material.

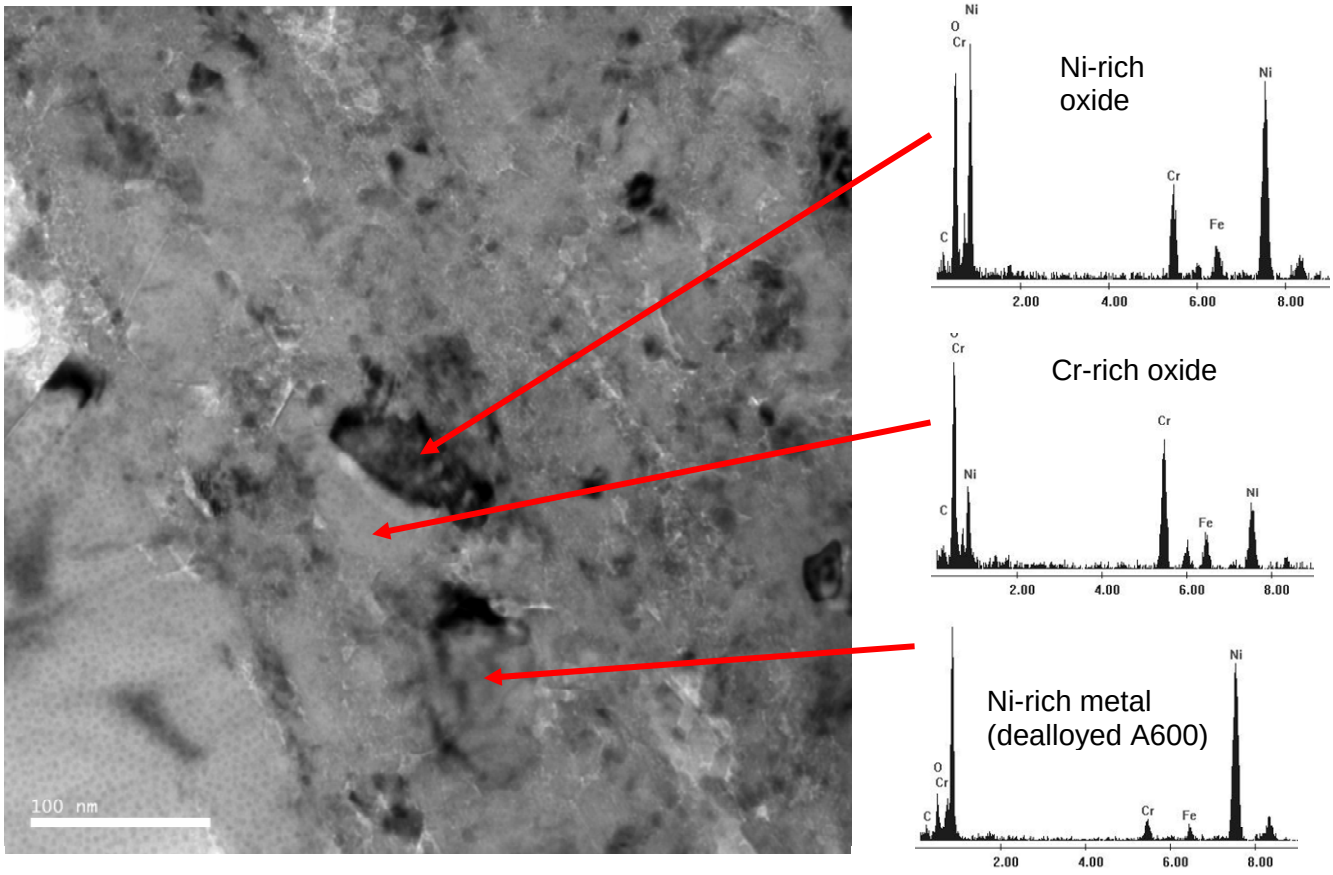

3.6.2 SCC Growth Rate Specimens

Hydrogenated water exposed Alloy 600 SCC growth rate specimens exhibit sharp crack tips with crack tip radii of ~ 2-3 nm [7,10,11] and with little general corrosion (Figure 20). Crack paths are intergranular with no evidence of cracking along slip planes or off the grain boundary and proceeded around Cr_7C_3 carbides. A thin layer (~ 20 nm) of Cr-rich oxide is observed along the carbide/matrix interface and no oxidation of carbides ahead of the crack tips is noted.

Figure 20. AEM Bright Field Image Showing an Intergranular SCC Crack Tip. Note the sharpness of the crack-tip. X-ray spectra from the oxide within the crack shows the variation in elemental constituents near the SCC crack tip. (high purity hydrogenated water, 640°F -338°C-).

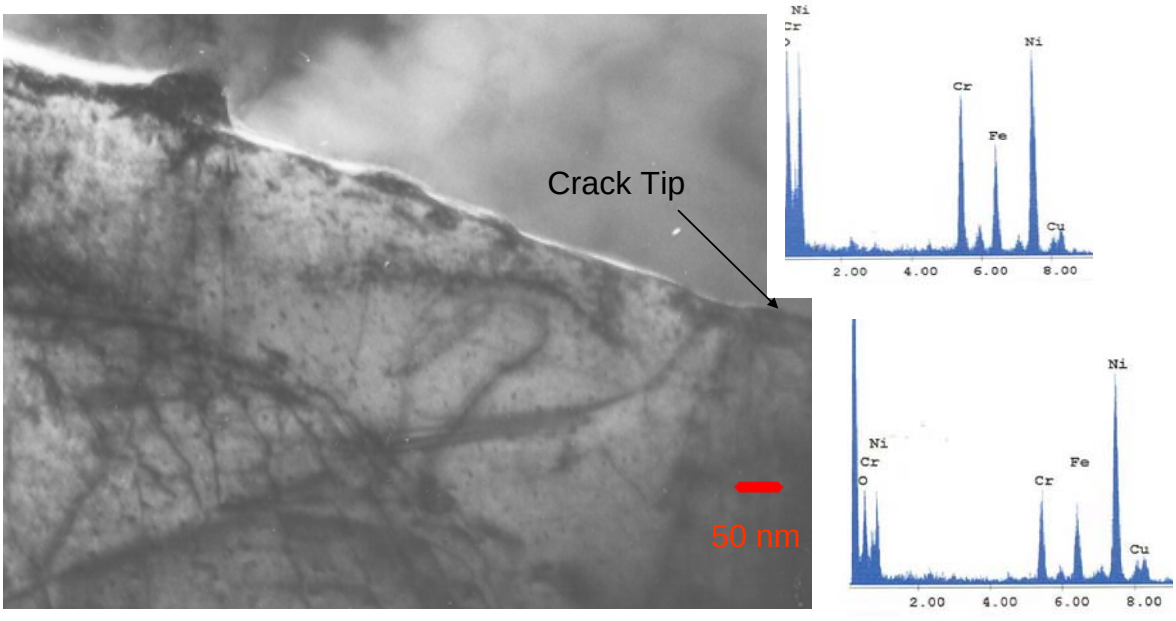

In contrast to the duplex oxide layers that are observed on bulk surfaces (e.g., corrosion coupons), Alloy 600 SCC crack tip and crack wake oxides consist of single layered oxides. NiO structure and spinel structure oxides are observed [7,11]. It is important to note that both iron and chromium are observed in the NiO structure oxide. Chromium rich spinels (e.g., $NiCr_2O_4$) are also observed, with the Cr rich spinel being the most common spinel phase. The high resolution AEM image in Figure 21 shows a Cr-rich, spinel structure oxide embedded in the NiO structure oxide near the crack tip in a specimen tested at 120 cc/kg hydrogen. Spinel oxides were more readily observed when specimens were tested within the nickel metal regime. NiO structure oxides are observed at all hydrogen levels.

No clear evidence of selective oxidation was apparent, either ahead of the crack tip or on small cracks emanating from the main crack. Additionally, no evidence of voids ahead of the crack tip was observed.

Figure 21. AEM High Magnification Image Near an SCC Crack Tip Region Showing Very Fine Grain Oxide Area 1 and Larger Oxide Crystal Area 2. X-ray spectrum 1 and 2 from area 1 and 2 show Ni rich oxide with elemental ratios similar to the base metal and larger oxide with roughly equal Fe, Cr and Ni (120 cc/kg hydrogenated water, 640°F -338°C-).

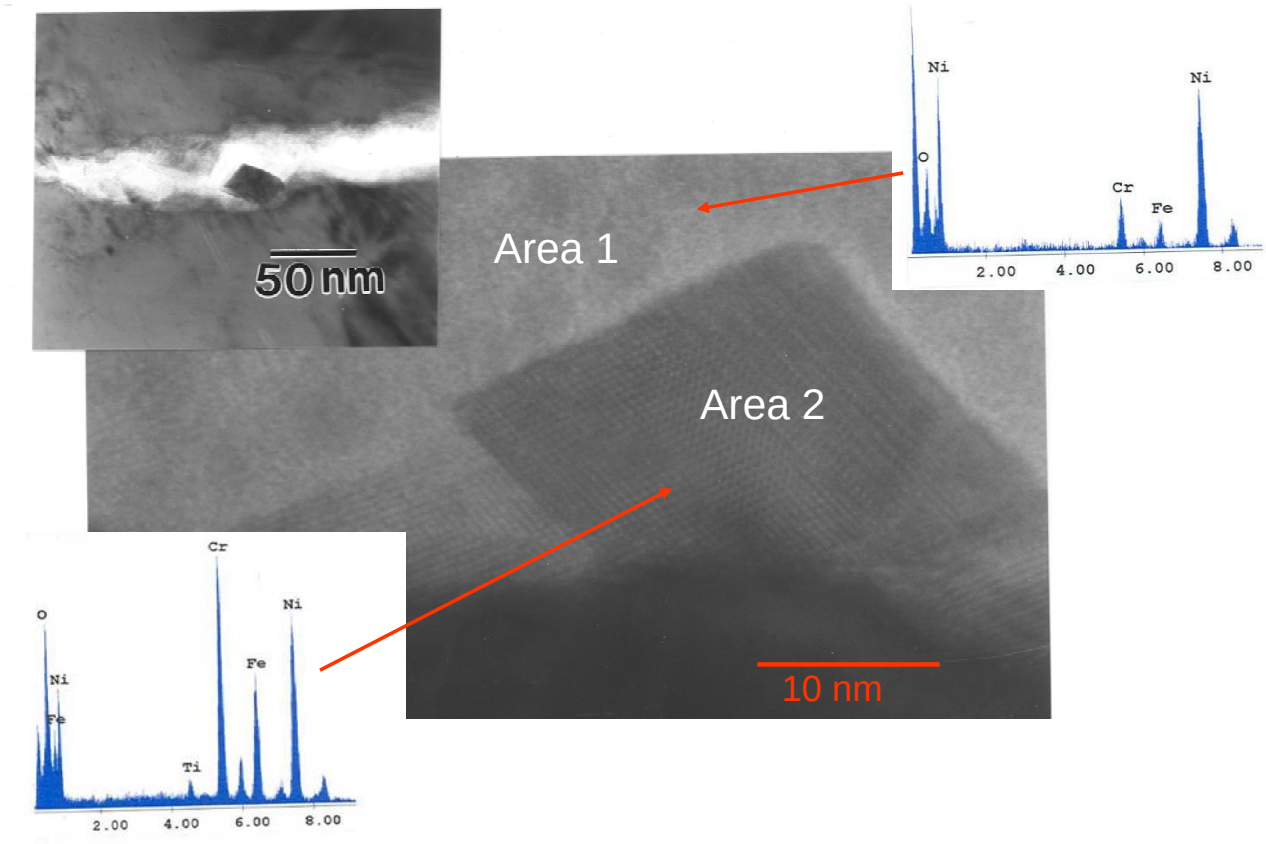

3.7 Implications of the Temperature Dependency of Corrosion to SCC

A comparison between the Table 5 corrosion data at 550°F and 640°F indicates that the thermal activation (Q) of Alloy 600 corrosion is approximately 30 kcal/mol. The similarity between the thermal activation energy of SCC, 33 kcal/mol [3], and the thermal activation of corrosion measured in this study suggests that 1) corrosion could be the rate controlling step in primary water SCC or 2) that corrosion and SCC have a common rate controlling subprocess. *Prior work [12, 13] suggests that hypothesis 2 (corrosion and SCC have a common rate controlling subprocess) is more likely.* Hypothesis 1 is unlikely since testing [12,13] has identified that nickel alloy primary water corrosion and SCC often show different key parameter dependencies. Specifically, Reference [12] showed a difference between the SCC and corrosion coolant hydrogen dependency of Alloy X-750, Figure 22. Reference [13] test results, additionally, showed a significant difference in the corrosion performance between specimens solution annealed before and after machining but no difference in the SCC initiation performance, Figure 23.

Figure 22: Comparison between the SCC and Corrosion Coolant Hydrogen Dependencies of Alloy X-750 in the HTH Condition at 680°F. Note a different functionality is observed suggesting that corrosion is not the rate controlling step in SCC, [12]. (ESCA corrosion film thickness measurements were performed on the external surface of the three noted compact tension crack growth rate specimens).

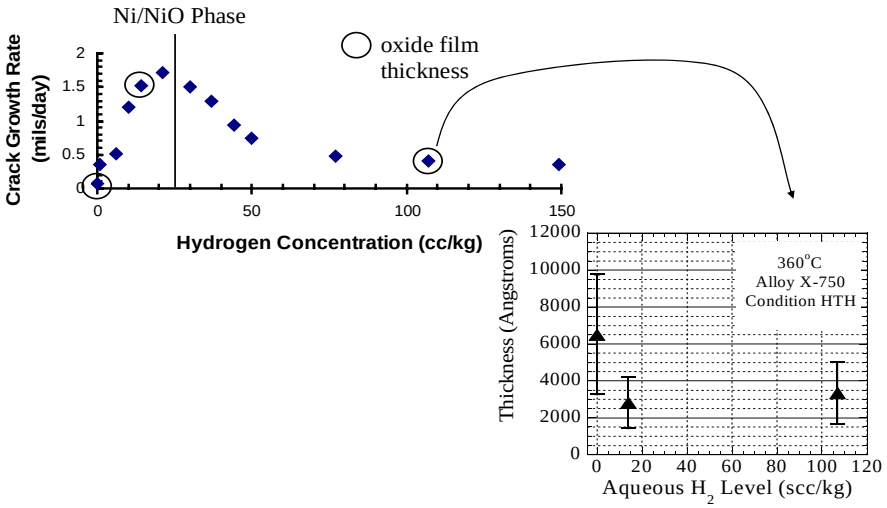

Figure 23: Comparison Between the Corrosion and SCC Performance of SA Specimens Heat Treated Before and After Machining: No difference in SCC initiation but significant corrosion differences [13].

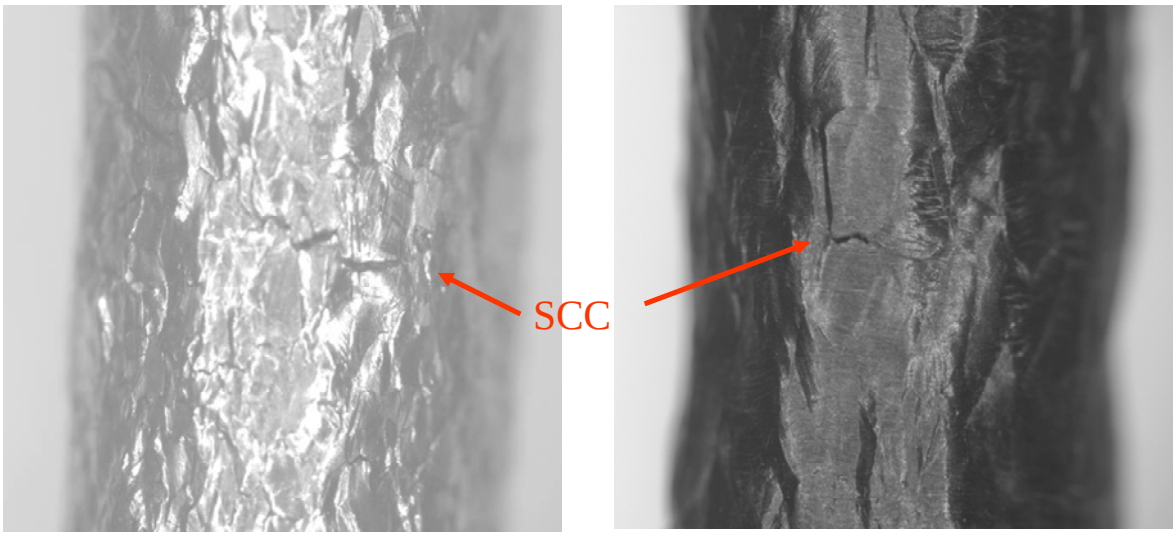

Tensile specimen machined then solution annealed at 2100°F for 20 minutes in vacuum with Ar quench

Material solution annealed at 2100°F for 20 minutes in vacuum with water quench then tensile specimen machined

If indeed corrosion and SCC have a common rate controlling subprocess then the common subprocess is likely the egress of oxidized cations through the developing oxide or the ingress of oxygen/water through the developing oxide. The egress of cation is viewed to be more probable since cation diffusion is the more likely nickel alloy corrosion rate controlling step [8]. A key subprocess in the proposed internal oxidation nickel alloy SCC mechanism [14] is oxygen ingress. The thermal activation energy results from this study are therefore consistent with the internal oxidation mechanism of primary water nickel alloy SCC. However, the Alloy 600 bulk surface and SCC corrosion oxide film morphology and composition data of this study suggests a non-selective oxidation process that is inconsistent with an internal oxidation mechanism of nickel alloy SCC.

4.0 CONCLUSIONS

- Testing in this study has shown that the thermal activation energy of Alloy 600 corrosion is ~30 kcal/mol. The similarity between the thermal activation energy of SCC, 33 kcal/mol [3], and the thermal activation energy of corrosion suggests that corrosion and SCC have a common rate controlling subprocess. Since nickel alloy primary water corrosion and SCC often show different key parameter dependencies, corrosion alone does not control SCC. Cation diffusion (most likely) and oxygen ingress are possible common rate controlling subprocesses.

- Analytical investigations of the structure and composition of Alloy 600 bulk surface corrosion product oxides produced in hydrogenated primary water revealed a duplex (inner and outer) oxide layer structure. The outer layer is a discontinuous layer comprised of relatively large (1 to 3 μm) nickel rich ferrite crystals and smaller (~0.1 μm) more chromium rich ferrite crystals. The inner "protective" layer consists of a fine grain chromium rich oxide (chromite spinel or Cr_2O_3). The inner layer of electrochemically polished and solution annealed specimens was a continuous chromite spinel of uniform composition. The inner layer of as-machined specimens formed within an original fine grain (subcell) machine deformation layer and was comprised of oxidized (chromite spinel, Cr_2O_3), dealloyed Alloy 600 (highly enriched Ni metal) and unoxidized material. Cr_2O_3 was only observed in specimens tested at 640°F (338°C). These results suggest that Cr_2O_3 forms more readily at elevated temperature. In this study a uniform layer of Cr_2O_3 was not present indicating non-selective oxidation.

- Test results have shown that electrochemically polished and solution annealed surface treatments reduces the extent of corrosion. Additionally, the outer layer ferrite deposits which form on these surfaces are adherent, and are oriented with respect to the underlying grain structure. In contrast the outer ferrite layer that forms on as-machined surfaces is not adherent and not orientated with the underlying metal grain orientation.

- In contrast to the duplex oxide layers that are observed on bulk surfaces, Alloy 600 SCC crack tip and crack wake oxides are single layered oxides. NiO structure and spinel structure oxides are observed. Iron and chromium are observed within the NiO structure oxide. SCC initiation specimen corrosion oxides are analogous to as-machined corrosion coupon oxide films.

5.0 REFERENCES

1. H Coriou et al., 3-eme Colloque de Metallurgie sur la Corrosion, Saclay North Holland Publ. Co., Amsterdam, Holland, p. 161, 1959.
2. DS Morton, SA Attanasio, and GA Young, "Primary Water SCC Understanding and Characterization Through Fundamental Testing in the Vicinity of the Nickel/Nickel Oxide Phase Transition", *Proceedings of the Tenth International Conference on Environmental Degradation of Materials in Nuclear Power Systems - Water Reactors*, Lake Tahoe, NV, ANS, 2001.
3. DS Morton, SA Attanasio, E. Richey and GA Young, "In Search of the True Temperature and Stress Intensity Factor Dependencies of PWSCC", *Proceedings of the Twelfth International Conference on Environmental Degradation of Materials in Nuclear Power Systems - Water Reactors*, Salt Lake City , UT, TMS, 2005.
4. P. Combrade et al., "Oxidation of Ni Base Alloys in PWR Water: Oxide Layers and Associated Damage to the Base Metal", *Proceedings of the Twelfth International Conference on Environmental Degradation of Materials in Nuclear Power Systems - Water Reactors*, Salt Lake City , UT, TMS, 2005.
5. Fabio Scenini et al., "Alloy Oxidation Studies Related to PWSCC", *Proceedings of the Twelfth International Conference on Environmental Degradation of Materials in Nuclear Power Systems - Water Reactors*, Salt Lake City , UT, TMS, 2005.
6. E. Richey, DS Morton, and MK Schurman, "SCC Initiation Testing of Nickel Based Alloys Using In-Situ Monitored Uniaxial Tensile Specimens", *Proceedings of the Twelfth International Conference on Environmental Degradation of Materials in Nuclear Power Systems - Water Reactors*, Salt Lake City, Utah, TMS, 2005.
7. N. Lewis et al., "Stress Corrosion Crack Growth Rate Testing and Analytical Electron Microscopy of Alloy 600 as a Function of Pourbaix Space and Microstructure", *Chemistry and Electrochemistry of Corrosion and Stress Corrosion Cracking: A Symposium Honoring the Contributions of RW Staehle, 2001 TMS Annual Meeting*, New Orleans, LA, 2001.
8. J. Robertson, "The Mechanism of High Temperature Aqueous Corrosion of Stainless Steels", Corrosion Science, Vol. 31, 1991.
9. DH Lister, RD Davidson and E McAlpine, Corrosion Science, Volume 27, pg 113, 1987.
10. SM Bruemmer, VY Gertsman and LE Thomas, "High Resolution AEM Comparison of Primary and Secondary-Side Intergranular Degradation in Alloy 600 Steam Generator Tubing", Corrosion/2000, Paper 196.
11. JS Fish et al., "AEM Investigations of Primary Water SCC in Nickel Alloys", *Proceedings of the Eighth International Conference on Environmental Degradation of Materials in Nuclear Power Systems - Water Reactors*, Amelia Island, FL 1997.
12. DS Morton et al., "The Influence of Dissolved Hydrogen on Nickel Alloy SCC: A Window to Fundamental Insight", Corrosion 2001 NACE Conference, Paper 01117, April 2001.
13. E Richey, DS Morton and RA Etien, "SCC Initiation Testing of Nickel Based Alloys in Primary", this conference.
14. PM Scott and M. Le Calvar, "Some Possible Mechanisms of Intergranular Stress Corrosion Cracking of Alloy 600 in PWR Primary Water", *Proceedings of the Sixth International Conference on Environmental Degradation of Materials in Nuclear Power Systems –Water Reactors*, San Diego, CA, 1993.